JACS
JOURNAL OF THE AMERICAN CHEMICAL SOCIETY
pubs.acs.org/JACS

Article

Electrochemical N−N Oxidatively Coupled Dehydrogenation of 3,5-Diamino-1*H*-1,2,4-triazole for Value-Added Chemicals and Bipolar Hydrogen Production

Jiachen Li,[▽] Yang Li,[▽] Yuqiang Ma, Zihang Zhao, Huarong Peng, Tao Zhou, Ming Xu,* Daidi Fan, Haixia Ma,* Jieshan Qiu,* and Zhengxiao Guo*

Cite This: *J. Am. Chem. Soc.* 2025, 147, 9505−9518

Read Online

ACCESS | Metrics & More | Article Recommendations | Supporting Information

ABSTRACT: Electrochemical H_2 production from water favors low-voltage molecular oxidation to replace the oxygen evolution reaction as an energy-saving and value-added approach. However, there exists a mismatch between the high demand for H_2 and slow anodic reactions, restricting practical applications of such hybrid systems. Here, we propose a bipolar H_2 production approach, with anodic H_2 generation from the N−N oxidatively coupled dehydrogenation (OCD) of 3,5-diamino-1*H*-1,2,4-triazole (DAT), in addition to the cathodic H_2 generation. The system requires relatively low oxidation potentials of 0.872 and 1.108 V vs RHE to reach 10 and 500 mA cm^{-2}, respectively. The bipolar H_2 production in an H-type electrolyzer requires only 0.946 and 1.129 V to deliver 10 and 100 mA cm^{-2}, respectively, with the electricity consumption (1.3 kWh per m^3 H_2) reduced by 68%, compared with conventional water splitting. Moreover, the process is highly appealing due to the absence of traditional hazardous synthetic conditions of azo compounds at the anode and crossover/mixing of H_2/O_2 in the electrolyzer. A flow-type electrolyzer operates stably at 500 mA cm^{-2} for 300 h. Mechanistic studies reveal that the Pt single atom and nanoparticle ($Pt_{1,n}$) optimize the adsorption of the S active sites for H_2 production over the $Pt_{1,n}$@VS_2 cathodic catalysts. At the anode, the stepwise dehydrogenation of $-NH_2$ in DAT and then oxidative coupling of −N−N− predominantly form azo compounds while generating H_2. The present report paves a new way for atom-economical bipolar H_2 production from N−N oxidative coupling of aminotriazole and green electrosynthesis of value-added azo chemicals.

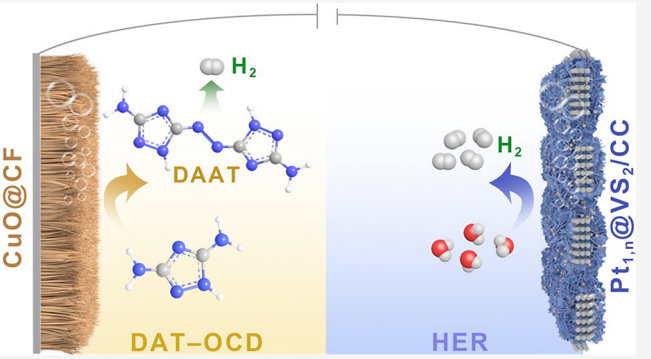

INTRODUCTION

Water electrolysis is an environmentally friendly pathway for hydrogen production, but direct coupling of the oxygen evolution reaction (OER) with the hydrogen evolution reaction (HER) results in several drawbacks. First, the anodic OER is thermodynamically unfavorable and sluggish due to the four-electron kinetic steps, responsible for 90% of the overall electricity consumption in water electrolysis.[1−3] The practical input cell voltage exceeds 1.8 V with a high electricity consumption of ∼5 kWh/m^3 of H_2.[4,5] Second, there is a high level of risk of H_2 and O_2 mixing, and thus, an expensive ion-exchange membrane is required to prevent gas crossover.[6] Third, the anodic product, O_2, is of low economic value. Finally, the anodic OER can also cause membrane degradation during the formation of reactive oxygen species.[7] Hence, the alternative strategies of coupling thermodynamically more favorable oxidation reactions to replace the OER have been widely investigated in recent years. The substrate molecules include alcohols,[8−10] aldehydes,[4,11,12] and amines[13−15] for upgrading to value-added chemicals. Other substrate molecules, such as urea,[16−18] hydrazine,[19−22] and sulfion,[23,24] are considered for green electrochemical degradation of pollutant substances. Despite the significant advances in the coupled water electrolysis systems, these strategies are still in the infant stages of development and there are still important tasks to undertake: (1) to design cell configurations to meet the industrial-scale current densities (reach up to 500 mA cm^{-2}); (2) to explore new green electrochemical pathways for pharmaceutical, energetic, and special chemicals;[7,25] and (3) to produce H_2 at both the cathode and the anode, so as to resolve the market-size mismatch between cathodic hydrogen production and anodic organic oxidation reaction.[4,11,12,26]

Azo compounds are ubiquitous for wide applications such as organic dyes, pigments, therapeutic reagents, and energetic

Received: December 3, 2024
Revised: February 28, 2025
Accepted: March 3, 2025
Published: March 8, 2025

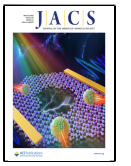

Scheme 1. Schematic Illustration of the Traditional Three-Step Pathway to Synthesize DAAT ECs and the One-Step Green Electrochemical Pathway to Synthesize DAAT, Coupled with HER for Low-Energy Value-Added Hydrogen Production

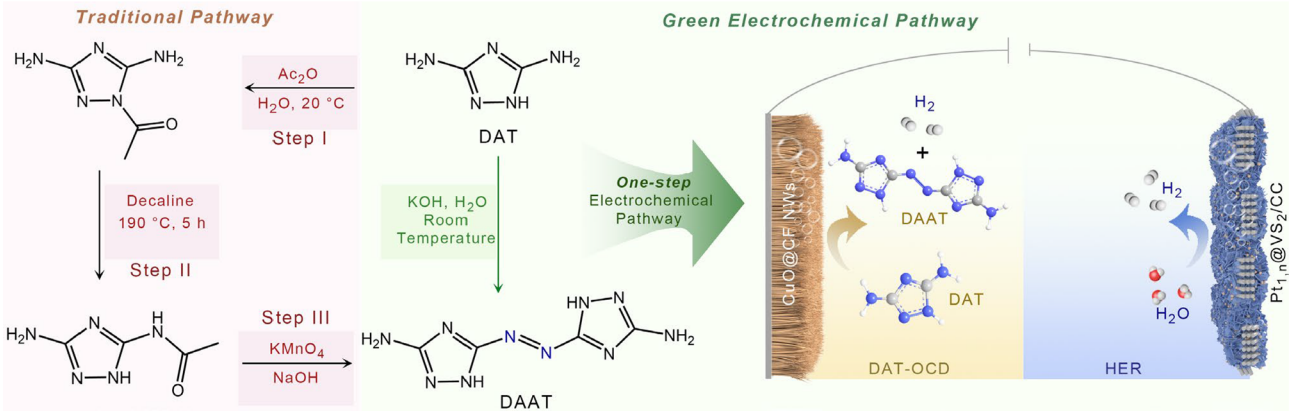

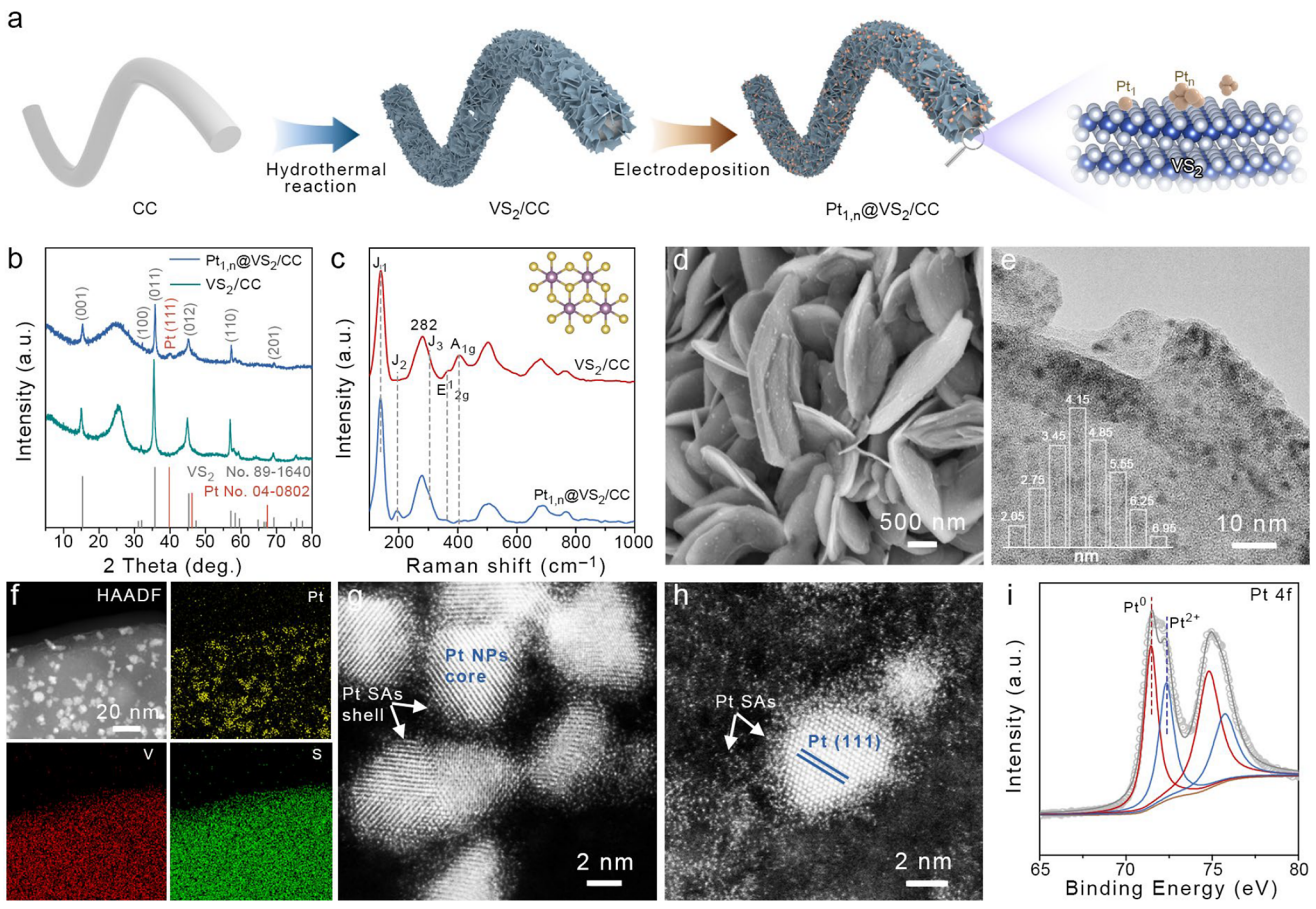

Figure 1. (a) Schematic illustration of the synthesis procedures for $Pt_{1,n}@VS_2/CC$. (b,c) XRD patterns and Raman spectra of $Pt_{1,n}@VS_2/CC$ and VS_2/CC. (d) SEM, (e) TEM, and (f) HAADF-STEM images of $Pt_{1,n}@VS_2$. Inset of (e): size distribution diagram of Pt NPs. (g,h) AC-HAADF-STEM images of $Pt_{1,n}@VS_2$. (i) High-resolution XPS spectrum of the Pt 4f signal for $Pt_{1,n}@VS_2/CC$.

materials.[27] Amino triazoles are regarded as good energy-containing compounds with excellent thermal performance, stability, and high density.[28−30] However, the traditional route of synthesizing azo compounds usually involves a high processing temperature and toxic/heavy metal reactants, accompanied by numerous steps; a viable alternative is the use of an electrochemical strategy.[31,32] Organic electrochemistry can avoid the use of hazardous reagents and complex synthetic procedures, and it consumes only electrical energy, which increasingly comes from low-cost renewable sources.[33] Hence, this work proposes a one-step electrochemical N−N oxidative-coupling dehydrogenation (OCD) of 3,5-diamino-1*H*-1,2,4-triazole (DAT-OCD) to synthesize 5,5′-diamino-3,3′-azo-1*H*-1,2,4-triazole (DAAT) compounds, while generating hydrogen from both electrodes, as outlined in the following.

The conventional synthetic process of DAAT usually involves several steps of acylation, thermal isomerization, and azo-bridging (Scheme 1),[29,34] which is energy-intensive and environmentally harmful. The proposed one-step electro-

https://doi.org/10.1021/jacs.4c17225
J. Am. Chem. Soc. 2025, 147, 9505−9518

chemical pathway of synthesizing DAAT in an aqueous solution can effectively avoid these drawbacks and improve atom economy, with the added value of the conversion with bipolar hydrogen production.

Moreover, the N−N oxidative coupling to azo bonds are thermodynamically more favorable (around 0.5 V vs RHE) than OER (1.23 V vs RHE), which is a much more desirable alternative to OER in terms of voltage efficiency and selectivity engineering.[35,36] The resultant hydrogen intermediates may be directly recombined to hydrogen gas via the Tafel mechanism (*H + *H → H_2) rather than the Volmer oxidation (*H + OH^- → * + H_2O + e^-) at a relatively low potential.[4] Based on this concept, we proposed the replacement of the OER with DAT-OCD, which is then coupled with HER to create a hybrid water electrolysis system (Scheme 1). The integrated system is expected to generate hydrogen gas from both the anode and the cathode, along with the value-added DAAT compound at a relatively low electricity power input.

To realize all of the benefits, catalyst design is essential for reducing the overpotential and increasing the energy conversion efficiency of water electrolysis. Single-atom catalysts (SACs) play a crucial role in significantly increasing the atomic utilization efficiency, but are often limited by an insufficient number and inadequate type of active centers, as well as the lack of neighboring sites for catalyzing multistep/electron reactions.[37−39] Particularly, alkaline HER involves water dissociation (Volmer) and hydrogen recombination (Tafel/Heyrovsky) steps. The SACs still suffer from low active site densities, usually leading to unsatisfactory activity for multistep alkaline HER.[39,40] Introducing nanoclusters (NCs) into SACs has been demonstrated as an efficient method for providing abundant cooperative active sites for alkaline HER.[41−43] Currently, SACs/NCs dispersed on various carbon-based substrates have emerged as mainstream heterogeneous catalysts.[44−47] Compared with carbon-based substrates, the transition metals in transition metal dichalcogenides (TMDs) provide more versatile and flexible coordination environments to regulate the catalytic activity of alkaline HER.[48]

Here, platinum single atoms and nanoparticles (Pt_1 and Pt_n) were synthesized over metallic vanadium disulfide nanosheets ($Pt_{1,n}$@VS_2) for the cathodic HER in the hybrid water electrolysis system. As the Group 5 metal disulfide, VS_2 shows an activated basal plane with intrinsically metallic features due to its relatively low unoccupied states (ε_{LUS} < −5.8 eV), which is a key descriptor for selecting basal-plane-active electrocatalysts.[49] In our electrocatalyst system, the core anchoring Pt_1 and the neighboring Pt_n can synergistically optimize the electronic structure of VS_2 to promote the HER activity, even superior to the commercial Pt/C, to reach a high current density (>100 mA cm^{-2}). The integrated hybrid water electrolysis system of DAT-OCD and HER showed ultralow cell voltages of 0.946 and 1.129 V for bipolar hydrogen production to reach 10 and 100 mA cm^{-2}, respectively, and delivered a low electricity consumption of 1.3 kWh per m^3 H_2 at an evaluated current density of 100 mA cm^{-2}. Meanwhile, the value-added DAAT solid compound was successfully generated on the anode side. The assembled flow device of the hybrid electrolysis system maintained stable catalysis over 300 h at 500 mA cm^{-2}, revealing its excellent tolerance and stability for industrial hydrogen production and value-added chemical cogeneration. This study paves a promising avenue for energy-saving bipolar hydrogen production and environmentally friendly synthesis of azo-triazole chemicals (Figures 1−4).

RESULTS AND DISCUSSION

Synthesis and Characterization of Cathodic HER Catalysts. Before the assembly of the hybrid water electrolysis system with DAT-OCD and HER, the cathodic and anodic electrocatalysts were first designed. The $Pt_{1,n}$@VS_2 supported on conductive carbon cloth ($Pt_{1,n}$@VS_2/CC) as the cathodic HER catalysts was prepared by a two-step process. The procedures involve a hydrothermal reaction to support VS_2 nanosheets (VS_2 NSs) on the CC substrate followed by electrodeposition of Pt NPs and Pt SAs on VS_2 NSs (Figure 1a).

Scanning electron microscopy (SEM) shows a vertical and staggered alignment of the VS_2 NSs on the CC substrate (Figure S1). Transmission electron microscopy (TEM) and high-resolution TEM (HRTEM) show that the lattice distance is 0.278 nm, corresponding to the (100) crystal plane of VS_2 (Figure S2a,b). High-angle annular dark-field scanning transmission electron microscopy (HAADF-STEM) and elemental mappings of VS_2 are performed to reveal the homogeneous distribution of V and S on the VS_2 NSs (Figure S2c−e). X-ray diffraction (XRD) patterns indicate that all of the diffraction peaks are assigned to the (001), (100), (011), (012), (110), and (201) planes of 1T-type VS_2 (JCPDS No. 89-1640).[50] After the deposition of $Pt_{1,n}$, the main diffraction peaks of $Pt_{1,n}$@VS_2/CC are almost identical to those of VS_2/CC with only a small new peak located at ∼39.7°, which may be ascribed to the Pt (111) plane (JCPDS No. 04-0802).[41] This result indicates that the electrodeposition of $Pt_{1,n}$ did not change the structure of the VS_2 substrate, and only a trace amount of $Pt_{1,n}$ is loaded over VS_2 (Figure 1b).

The inductively coupled plasma results confirm that the contents of Pt and V in $Pt_{1,n}$@VS_2 are 0.128 mg_{Pt} cm^{-2} and 1.22 mg_V cm^{-2}. The Raman spectra further verified the crystal structure of $Pt_{1,n}$@VS_2. As shown in Figure 1c, the characteristic vibration bands of VS_2/CC at approximately 141, 282, 304, 367, and 406 cm^{-1} are assigned to the J_1, E_g, J_3, E^1_{2g}, and A_{1g} vibrational modes of the octahedral (1T) phase of VS_2, respectively, with some trigonal prismatic (2H) phase of VS_2 coexisting in the samples.[51] Interestingly, the deposition of $Pt_{1,n}$ (if there is no special illustration, $Pt_{1,n}$@VS_2/CC is indicated as Pt-2.0 with the optimal Pt ion content of 2.0 mL; the detailed influence of the Pt ion concentration on the HER performance is shown in Figure 4) induces the disappearance of the A_{1g} mode and is accompanied by a fresh peak at ∼195 cm^{-1} corresponding to the J_2 mode of 1T-VS_2. This result may be due to the transformation of 2H to 1T-VS_2 during the electrodeposition of $Pt_{1,n}$. We speculate that such a special electrochemical reduction environment could introduce S-vacancies and inject electrons to the S−V−S framework, and the phase transformation is triggered.[52,53]

The sulfur vacancies in $Pt_{1,n}$@VS_2/CC are further supported by electron paramagnetic resonance (EPR). Compared with VS_2/CC, a strong paramagnetic absorption signal is observed at g = 2.001 for $Pt_{1,n}$@VS_2/CC, referring to the unpaired electrons being trapped in sulfur vacancies (Figure S3).[54] After the electrodeposition of $Pt_{1,n}$ on VS_2/CC, the morphological changes of nanosheets are not observed in the SEM image. Some nanoparticles are homogeneously dispersed on the nanosheets, indicating the successful loading of $Pt_{1,n}$ on VS_2/CC (Figures 1d and S4). Although in the HRTEM image of

https://doi.org/10.1021/jacs.4c17225
J. Am. Chem. Soc. 2025, 147, 9505−9518

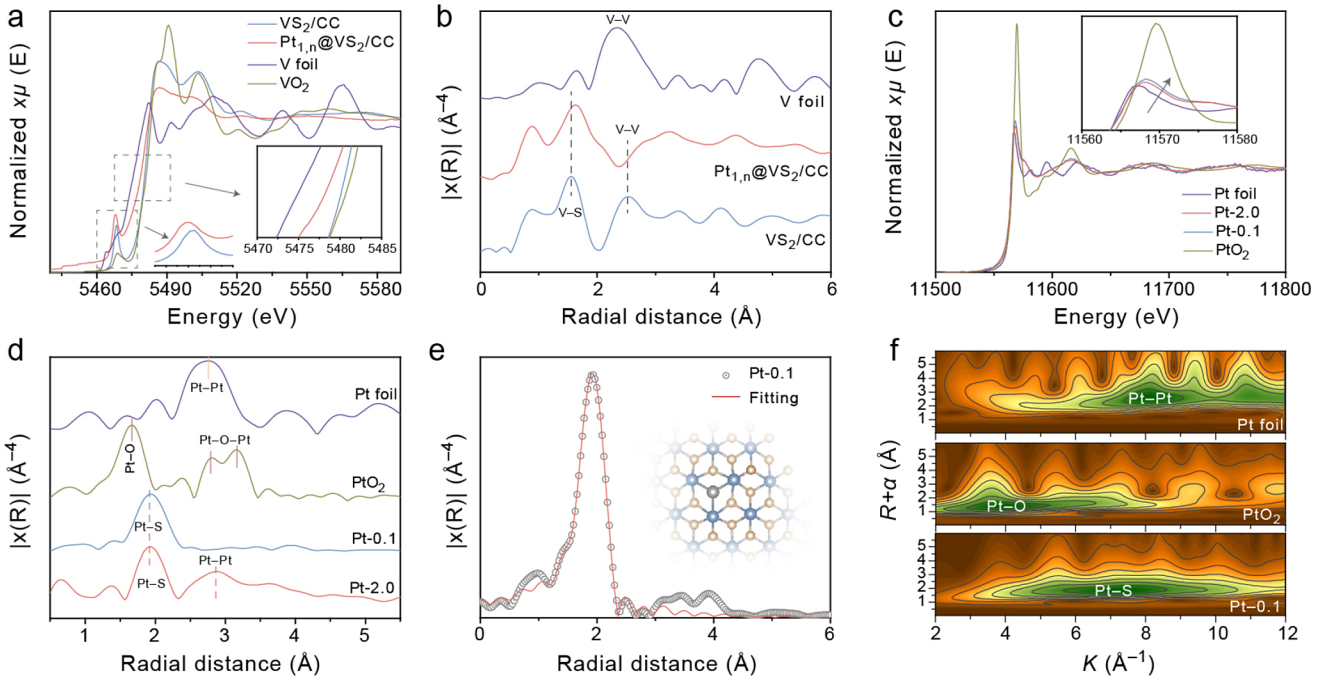

Figure 2. (a) Normalized XANES at the V *K*-edge for VS_2/CC, $Pt_{1,n}$@VS_2/CC, and reference samples. (b) k^3-weighted FT-EXAFS of the V *K*-edge for the samples. (c) Normalized XANES at the Pt L_3-edge for Pt-0.1, Pt-2.0, and the reference samples. (d) k^3-weighted FT-EXAFS of Pt L_3-edge for the samples. (e) Fitting curve of FT-EXAFS of the Pt L_3-edge for Pt-0.1. (f) Wavelet transformation (WT) for the FT-EXAFS of the Pt L_3-edge for Pt-0.1.

$Pt_{1,n}$@VS_2, small dark nanoparticles with an average diameter of 4.31 nm are uniformly dispersed on the VS_2 NSs, the corresponding HAADF-STEM images, EDS spectra, and elemental mappings indicate that these are Pt NPs on the VS_2 surface (Figures 1e,f and S5). However, further information on Pt on VS_2 NSs can be collected by AC HAADF-STEM, where the Pt NPs (core) and Pt SAs (shell) coexist to form a novel core−shell structure (Figure 1g,h). The lattice distance of Pt NPs (0.226 nm) is indicative of the Pt (111) plane. The coexistence of Pt NPs and Pt SAs can provide multiple types of active sites for better promoting multistep kinetic reactions.[39]

X-ray photoelectron spectroscopy (XPS) results of the Pt 4f signal for $Pt_{1,n}$@VS_2/CC show two pairs of peaks located at 71.4/74.8 and 72.3/75.7 eV, respectively. The former can be attributed to metallic Pt^0, while the latter corresponds to Pt^{2+} (Figure 1i).[55] This result supports the coexistence of the dominant Pt NPs and Pt SAs in VS_2/$Pt_{1,n}$. High-resolution XPS of V 2p and S 2p signals of the samples is carried out to uncover the electronic interaction of VS_2 and $Pt_{1,n}$. The V 2p spectra of VS_2/CC fitted with four peaks at 513.7, 521.2, 516.9, and 524.2 eV are assigned to V^{2+} $2p_{3/2}$, V^{2+} $2p_{1/2}$, V^{4+} $2p_{3/2}$, and V^{4+} $2p_{1/2}$, respectively.[56] After the deposition of $Pt_{1,n}$, the peaks shifted to a lower binding energy (*ca.* 0.15 eV), indicating that the loading of $Pt_{1,n}$ induces electron accumulation around V, and more metallic V with 1T-VS_2 are formed (Figure S6a). The same trend is also observed at the S 2p signal (Figure S6b). High-resolution S 2p XPS spectra of VS_2/CC show four spin−orbit peaks at 160.9/162.1 and 163.1/164.3 eV, ascribing to S^{2-} species and metal−sulfur excitation in VS_2, respectively.[57] Notably, the S^{2-} ratio in $Pt_{1,n}$@VS_2 is lower than that of VS_2, followed by a binding energy shift to a lower position (ca. 0.15 eV), which may be due to the electrochemical reduction conditions during the deposition of $Pt_{1,n}$ and the strong metal−support electronic interaction between $Pt_{1,n}$ and VS_2. The electron reconfiguration in $Pt_{1,n}$@VS_2 is able to regulate the adsorption strength of alkaline HER intermediates for promoting the catalytic activity.

X-ray adsorption spectroscopy was performed for further exploration of the local coordination environment and the electronic structure of $Pt_{1,n}$@VS_2. As shown in Figure 2a, the V *K*-edge X-ray absorption near-edge spectra (XANES) of VS_2/CC is similar to those of the VO_2 reference sample, indicating that the V atoms exhibit an oxidation state of +4. However, the deposition of $Pt_{1,n}$ induces a valence of V in VS_2 lower than +4, as evidenced by the location of the V *K*-edge XANES of $Pt_{1,n}$@VS_2/CC between VO_2 and V foil. The results further suggest that the loading of $Pt_{1,n}$ on VS_2 leads to electron transfer from $Pt_{1,n}$ to VS_2, which is in line with the XPS results. In addition, the intensity of pre-edge peak ($1s \rightarrow 3d$) of $Pt_{1,n}$@VS_2/CC increases compared with VS_2/CC, suggesting the phase conversion of 2H into the 1T phase of VS_2, which is in concert with the Raman result.[58]

In the V *K*-edge Fourier transform extended X-ray absorption fine structure (FT-EXAFS) spectra, the peaks at 1.56 and 2.55 Å are ascribed to the shell coordination of V−S and V−V bonds for VS_2/CC, respectively (Figure 2b).[59] Note that the multiple scattering of V−S peaks shift to a larger distance after the loading of $Pt_{1,n}$ on VS_2, resulting from the lattice tensile strain and breaking of the V−S bond to create abundant unsaturated coordinated S caused by the immobilization of $Pt_{1,n}$.[60,61] However, the second-shell V−V intensity of $Pt_{1,n}$@VS_2 shows an apparent decrease, suggesting the occurrence of structural disorder induced by atomic rearrangement after the doping of $Pt_{1,n}$.[61,62] The normalized Pt L_3-edge XANES spectra of Pt-0.1 (the content of Pt ions in the electrolyte is 0.1 mL) and Pt-2.0 are shown in Figure 2c, and the intensities of the white line for Pt-0.1 and Pt-2.0 are located

https://doi.org/10.1021/jacs.4c17225
J. Am. Chem. Soc. 2025, 147, 9505−9518

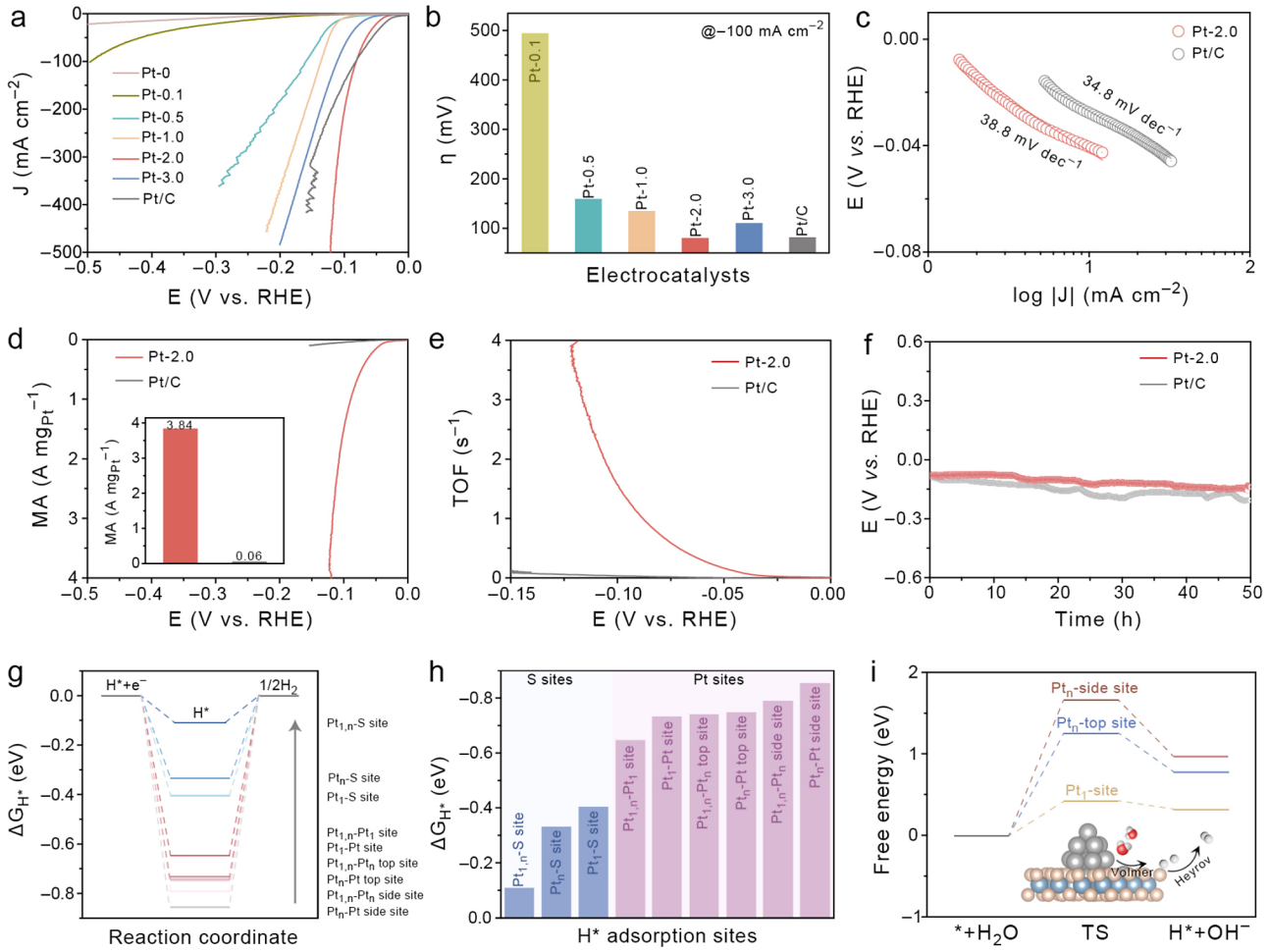

Figure 3. (a) LSV curves of $Pt_{1,n}$@VS_2/CC with different Pt^{4+} contents. (b) Comparison of the overpotential at −100 mA cm^{-2} for different $Pt_{1,n}$ loadings on VS_2/CC. (c) Tafel plots of Pt-2.0 and commercial Pt/C. (d,e) MS and TOF plots of Pt-2.0 and commercial Pt/C. (f) Long-term stability of Pt-2.0 and Pt/C at a current density of −100 mA cm^{-2}. (g) Calculated ΔG_{H^*} values at various sites of $Pt_{1,n}$@VS_2. (h) Comparison of ΔG_{H^*} on the S and Pt sites of Pt_1, Pt_n, and $Pt_{1,n}$. (i) Free energy of the water dissociation barrier on different sites (inset: schematic illustration of the proposed alkaline HER mechanism).

between the Pt foil and the PtO_2 reference samples, indicating that Pt atoms carry positive charges. However, the higher white-line intensity of Pt-0.1 and more positive edge shift of Pt-0.1 compared to that of Pt-2.0 are attributed to the higher content of positively charged Pt SAs in Pt-0.1. The ratio of Pt SAs to Pt NPs can be well controlled by adjusting the concentration of the Pt^{4+} solution before the electrodeposition of $Pt_{1,n}$ on VS_2. The formation of Pt SAs and Pt NPs in $Pt_{1,n}$ is further proved by the Pt L_3-edge FT-EXAFS spectra (Figure 2d). Pt-0.1 exhibits only one dominant peak located at 1.93 Å, assigned to Pt−S bonding, proving the single atomic dispersed form of Pt on VS_2 under a low concentration of Pt^{4+}. In addition to the Pt−S bond, the new peak centered at 2.88 Å in Pt-2.0 corresponds to the Pt−Pt bond. This result indicates that the increased concentration of the Pt^{4+} precursor could induce partial aggregation into nanoparticles and lead to the coexistence of Pt SAs and Pt NPs in $Pt_{1,n}$.

The EXAFS spectrum of Pt-0.1 was further treated by least-squares EXAFS curve-fitting analysis (Figure 2e). The average coordination numbers of Pt−S and Pt−V bonds are estimated to be 3.1 and 3.0. We can thus speculate that the Pt atoms may be immobilized in the S vacancy and coordinated with three V and S atoms (Table S1). The coordination environment of Pt in Pt-0.1 is then verified by wavelet transform (WT) analysis (Figure 2f). The WT reveals that the Pt bonding location can be speculated based on the spectral maximum intensity of the Pt−O bond in PtO_2 ($k \approx 3.98$ $Å^{-1}$) and the Pt−Pt bond in the Pt foil ($k \approx 8.09$ $Å^{-1}$). The result indicates that the weight of coordination elements is located between Pt and O such as S ($k \approx 7.19$ $Å^{-1}$), further supporting the Pt−S bonds in Pt-0.1.

Alkaline HER Tests and Cathodic Density Functional Theory (DFT) Calculations. The cathodic HER performance of the prepared $Pt_{1,n}$@VS_2/CC is the key reaction for an energy-efficient hybrid water electrolysis system. The influence of the Pt^{4+} concentration on the HER performance is first investigated by linear sweep voltammetry (LSV), and the corresponding overpotentials at a current density of −100 mA cm^{-2} (η_{100}) are recorded (Figure 3a,b). A notably lower η_{100} is obtained over the Pt-2.0 (81.3 mV) than those of Pt-0.1 (495 mV), Pt-0.5 (160 mV), Pt-1.0 (136 mV), Pt-3.0 (11.1 mV), and commercial Pt/C (81.9 mV). Under a current density of −10 mA cm^{-2}, Pt-2.0 still showed a low overpotential (η_{10}) of 40.3 mV, which is slightly higher than that of the commercial Pt/C (27.8 mV). However, Pt-2.0 delivers a steady current enhancement to a high current density (>100 mA cm^{-2}) with a gradually lower overpotential than that of the Pt/C.

Compared with the sharp fluctuation of the LSV curve under a high current density of Pt/C, a rather stable flat curve is

https://doi.org/10.1021/jacs.4c17225
J. Am. Chem. Soc. 2025, 147, 9505−9518

noted for Pt-2.0 under the same conditions, which may be attributed to the 3D self-supporting $Pt_{1,n}$@VS_2/CC nanosheet architecture, with the superhydrophilic surfaces allowing for faster bubble removal during HER.[63] The superhydrophilicity of Pt-2.0 is proven by the contact angle measurement (Figure S7). Compared with the CC substrate, the support of VS_2 and VS_2/$Pt_{1,n}$ increases the surface wettability with a contact angle of 0°, and the water droplet seeps through the entire matrix immediately, suggesting the superhydrophilic feature of the electrocatalyst. Such a unique nature could provide a more wettable surface to expel the generated H_2 gas bubbles and improve the cycling stability.

Tafel plots are obtained to determine the kinetic rate and possible mechanism of alkaline HER (Figure 3c). The Tafel slope of Pt-0 (VS_2/CC) is measured to be 142.8 mV dec^{-1}, indicating that the rate-determining step (RDS) of the Volmer process dominates the reaction. However, the loading of $Pt_{1,n}$ on VS_2/CC shows a significant decrease in the Tafel slope to 38.8 mV dec^{-1}, which is close to that of the commercial Pt/C (34.8 mV dec^{-1}). This result suggests the Volmer−Heyrovsky pathway, with the electrochemical H_2 desorption on $Pt_{1,n}$@VS_2/CC as the RDS.[64] It also reveals that the anchoring of $Pt_{1,n}$ sites may assist in reducing the energy barrier of the Volmer step to promote water dissociation and produce H* for the following Heyrovsky step; the speculation is further supported by DFT calculations, as discussed below. As both Pt SAs and Pt NPs coexist in $Pt_{1,n}$, potassium thiocyanate (KSCN) and ethylenediaminetetraacetic acid (EDTA) are introduced in the electrolyte, respectively. EDTA can block the single-atom site by coordination, while SCN^- deactivates both single atoms and nanoparticles by covering the surface of $Pt_{1,n}$.[65] As shown in Figure S8, the η_{10} of $Pt_{1,n}$@VS_2/CC delivers a negative shift by ca. 55 mV after the introduction of EDTA, while the η_{10} increases by only *ca.* 10 mV after the addition of KSCN. The poisoning results suggest that although Pt SAs and Pt NPs both deliver a highly efficient alkaline HER activity, Pt SAs play a dominant role.

The intrinsic activity and atomic utilization of $Pt_{1,n}$ are then evaluated by mass activity (MS) tests. Pt-2.0 exhibits an MS value of 1.55 A mg_{Pt}^{-1} at an overpotential of 100 mV, which is about 35 times higher than that of commercial Pt/C (0.04 A mg_{Pt}^{-1}) (Figure 3d). The turnover frequency (TOF) was determined to further evaluate the intrinsic activity of the catalysts. Pt-2.0 reaches a high TOF value of 1.57 s^{-1} at an overpotential of 100 mV, largely surpassing commercial Pt/C (0.04 s^{-1}, ∼34.5 times) (Figure 3e). Stability is another important factor that determines the lifetime of catalysts (Figure 3f). A catalyst should be operated at high current densities to meet the industrial demand. As a sharp comparison of Pt/C, the long-term stability test of the elaborate Pt-2.0 is performed over 50 h, which shows negligible decay of activity to reach a current density of −100 mA cm^{-2}.

DFT calculations were then performed to reveal the synergistic effect among the VS_2 substrate, Pt SAs, and Pt NPs. The structures of Pt_1 (Pt SA is located at the S vacancy of the VS_2 (002) plane), Pt_n (Pt_{13} NCs load on the VS_2 (002) plane), and $Pt_{1,n}$ (coexistence of Pt_1 and Pt_n) were constructed and then fully relaxed (Figure S9). All of the possible Pt or S active sites are considered in the H* adsorption free energy (ΔG_{H^*}) calculation. As a rule of thumb, an ideal HER catalyst delivers a thermoneutral value of ΔG_{H^*} close to zero.[66] Figure 3g displays the ΔG_{H^*} on various Pt and S sites of Pt_1, Pt_n, and $Pt_{1,n}$, and the corresponding ΔG_{H^*} values are collected and shown in Figure 3h (Figure S10). It is clear that the S site exhibits thermodynamics more favorable for H* adsorption than those of Pt sites. Especially, compared with the ΔG_{H^*} on S sites adjacent to Pt_n (−0.33 eV) or Pt_1 (−0.40 eV), the H* adsorption on S sites adjacent to $Pt_{1,n}$ shows the most favorable ΔG_{H^*} of −0.10 eV. This result indicates that the electron interactions between Pt_1 and Pt_n could modulate charge redistribution and achieve optimal binding strengths of H* on S active sites of $Pt_{1,n}$. To further clarify the specific active sites for hydrogen evolution, in situ surface-enhanced Raman spectroscopy (SERS) was performed across a potential range of 0 to −0.8 V vs. RHE (Figure S11a). When the potential became more negative, a Raman peak located at ca. 2580 cm^{-1} gradually appeared, and its intensity increased as the potential was further reduced to −0.8 V vs. RHE. Such a peak was ascribed to the stretching vibration of the S−H bond.[67−69] However, the Pt−H vibration located around 1990−2100 cm^{-1} does not exist, suggesting that the active sites for hydrogen formation are mainly contributed by the S sites in $Pt_{1,n}$@VS_2.[70,71] To further analyze the variation of the H* binding capacity with the S sites in $Pt_{1,n}$@VS_2, Pt_1@VS_2, and Pt_n@VS_2, we calculated the *p*-band centers (ε_p) of active S sites for H* adsorption since the H* adsorption capacity on the S sites of sulfides is closely related to the *p* electron states near the Fermi level.[72] As shown in Figure S11b, compared with Pt_1@VS_2 and Pt_n@VS_2, the ε_p of S on the $Pt_{1,n}$@VS_2 is further away from the Fermi level, indicating the electronic interaction of Pt SAs and Pt NPs jointly regulating the adsorption of H* on S sites, close to thermoneutrality. This result was in agreement with the ΔG_{H^*} discussed above.[73] On the other hand, the thermodynamic trends for water molecule dissociation of the Volmer step are critical to ensure the fast alkaline HER process. The energy barriers of the Volmer step on Pt_1 and Pt_n sites are calculated (Figures 3i and S12). The Pt_1 site meets a lower transition state energy of 0.43 eV compared to the Pt_n-top (1.26 eV) and Pt_n-side (1.67 eV) sites, indicating that the water molecules are more likely to dissociate on the Pt SA site. In addition, the weak bonding energy of the H_2O molecule on the S site of $Pt_{1,n}$ (0.93 eV) suggests that the S sites may not be the active sites for water dissociation (Figure S13). These results mean that Pt SAs are responsible for the decrease of the Tafel slope via the promotion of the Volmer step (water dissociation) after the loading of $Pt_{1,n}$, which is in agreement with the Pt ion concentration gradient and poison tests. DFT calculations revealed the cascade catalysis of alkaline HER and that the Pt SAs site promotes the Volmer step, and the produced H* spill over to the S sites via the Heyrovsky pathway for fast hydrogen production.

Anodic Electrochemical DAT-OCD Investigation. The high thermodynamic potential of the OER impels us to explore thermodynamically favorable and value-added alternative oxidation reactions for the reduction of energy consumption in water electrolysis systems. However, the key challenge of hybrid water electrolysis systems is the market-size mismatch between cathodic hydrogen production and the anodic oxidation product for large-scale deployment. The bipolar hydrogen production strategy-enabled hydrogen production at both the anode and the cathode could well overcome this challenge.[4] With this consideration in mind, we started investigating a thermodynamically favorable N−N oxidative coupling reaction of amino compounds to synthesize value-added azo chemicals. The CuO nanowire supported on 3D

https://doi.org/10.1021/jacs.4c17225
J. Am. Chem. Soc. 2025, 147, 9505−9518

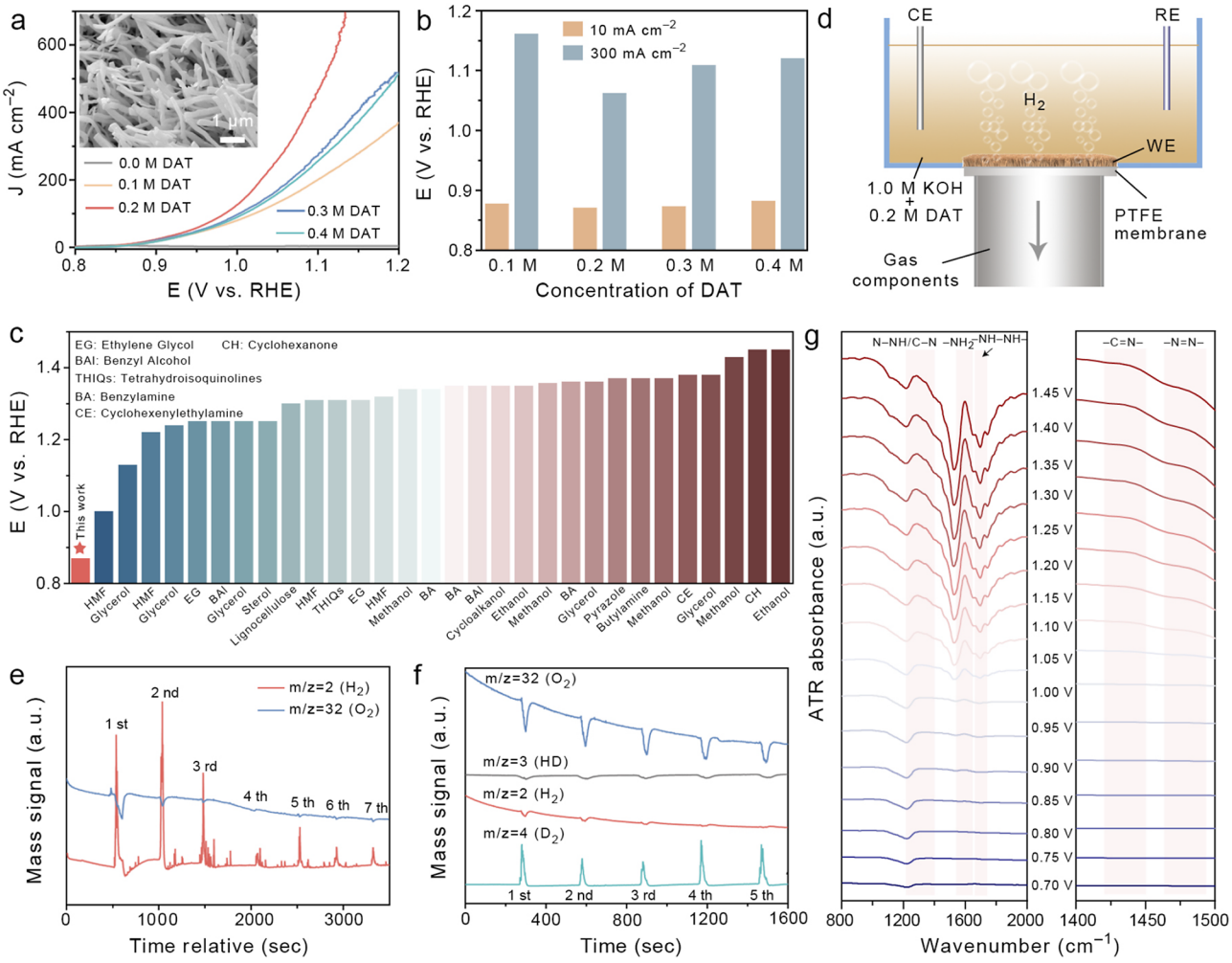

Figure 4. (a) LSV curves of DAT-OCD on CuO@CF NWs in various concentrations of DAT substrates. Inset: SEM image of CuO@CF NWs. (b) Bar graph of the collected potentials of DAT-OCD at the current densities of 10 and 300 mA cm^{-2} at different DAT concentrations. (c) Comparison of DAT-OCD potentials with the reported mainstream upgradation oxidation reactions to produce value-added chemicals at a current density of 10 mA cm^{-2}. (d) Schematic illustration of a DEMS reactor during the DEMS tests. (e) In situ DEMS tests of DAT-OCD for seven LSV cycles over specified potential ranges. (f) In situ DEMS tests of the deuterated DAT oxidation reaction for five LSV cycles. (g) In situ ATR-FTIR spectra of DAT-OCD over the specified potential ranges.

copper foam (CuO@CF NWs) was used as a model catalyst for DAT-OCD as the CuO-based catalysts are inert for competitive OER and active for organic small-molecule oxidation.[74]

CuO@CF was prepared by the calcination of $Cu(OH)_2$@CF NWs, obtained from in situ etching in alkaline liquor (Figure S14). The XRD pattern verifies the pure CuO supported on CF substrates (Figure S15). The DAT-OCD activities of CuO@CF and other Cu- or Ni-based benchmark catalysts are compared using LSV tests in 1.0 M KOH containing optimal 0.2 M DAT (Figures 4a and S16). The onset potential of DAT-OCD on CuO@CF is as low as 0.83 V vs RHE and delivers 0.87 and 1.06 V vs RHE to reach current densities of 10 and 300 mA cm^{-2}, respectively. These results are much lower than those of copper foam (1.21 V), $Cu(OH)_2$@CF NWs (1.38 V), and nickel foam (not up to the target current density) at 300 mA cm^{-2}, and the commercial Pt wire delivered a relatively low DAT-OCD activity.

In view of the low activity of the competing OER reaction and the excellent performance of the oxidation of organic small molecules on Cu-based catalysts, the emphasis was on the Cu-based catalysis for DAT-OCD.[4] The advantages of CuO@CF over other Cu-based catalysts were further studied by in situ attenuated total reflection Fourier transform infrared (ATR-FTIR) spectroscopy. In situ ATR-FTIR of DAT-OCD for CuO@CF, $Cu(OH)_2$@CF, and bare CF were comparatively assessed to evaluate the adsorption characteristics of the DAT substrate on Cu-based electrocatalysts so as to further clarify the advantages of DAT-OCD on the CuO@CF electrode (Figure S17). The characteristic peak at ∼1593 cm^{-1}, due to the stretching vibration of the $-NH_2$ group in DAT, represents the adsorbed DAT molecules on the catalysts.[75] The increased peak intensities can be attributed to a high density of the adsorbed substrate molecules on the catalyst surface, reflecting the strengthened adsorption capacity.[76,77] $Cu(OH)_2$@CF and the bare CF support showed a relatively weak adsorption peak of $-NH_2$, indicating a weak adsorption behavior for the DAT substrate. In contrast, a more pronounced peak at ∼1593 cm^{-1} was detected on CuO@CF, indicating the strong adsorption therein. In addition, the adsorption capacity of OH* on Cu-based catalysts was evaluated by in situ ATR-FTIR since the

https://doi.org/10.1021/jacs.4c17225
J. Am. Chem. Soc. 2025, 147, 9505−9518

reaction of DAT with OH* is crucial for subsequent dehydrogenation steps in DAT-OCD. As shown in Figure S18a, two peaks at ~3702 and ~3784 cm^{-1} during DATOR on CuO@CF can be assigned to the stretching vibrations of O−H.[78,79] The peak intensity becomes more pronounced with increasing applied potential. In contrast, the peak intensity of OH* was much weaker during DAT-OCD on bare CF and $Cu(OH)_2$@CF (Figure S18b,c). These results imply an enhanced interaction between OH* and the CuO@CF catalyst for promoting the dehydrogenation of DAT, compared with $Cu(OH)_2$@CF and bare CF. The above results indicate the superior activity of DAT-OCD on CuO@CF, relative to those on $Cu(OH)_2$@CF and CF.

The DAT-OCD activity of CuO@CF NWs under various DAT concentrations (0.1, 0.2, 0.3, 0.4 M) shows a volcano trend that the 0.2 M DAT delivers the highest activity at 10 mA cm^{-2} and high current density (300 mA cm^{-2}) (Figure 4b). The LSV curves also exhibit that the DAT-OCD could reach an industrial-level current density >500 mA cm^{-2}, revealing the potential for incorporating DAT-OCD in the anode of the hybrid water electrolysis system. The DAT-OCD activity with an ultralow working potential is superior to those of the state-of-the-art upgrading oxidation reactions, such as 5-hydroxymethylfurfural oxidation reaction,[80] glycerol oxidation,[81] methanol oxidation,[82] and ethanol oxidation[83] (Figure 4c). The optimal DAT concentration (0.2 M) was then used in subsequent DAT-OCD tests. Considering the low oxidation potential of DAT-OCD and the presence of reactive hydrogen atoms in the amino functional group of DAT, we postulate that the adsorbed hydrogen atom (H*) originating from the amino groups of DAT may undergo a Tafel recombination (H* + H* → H_2) to form H_2 rather than the large-kinetic-barrier Volmer pathway (H* + OH^- → H_2O + e^-).[4,12]

As a proof-of-concept, in situ differential electrochemical mass spectrometry (DEMS) was performed to quantify the amount of produced gas during DAT-OCD. As shown in Figure 4d, a three-electrode reaction tank was set up to perform the in situ DEMS, and the CuO@CF NWs as the working electrode was tiled on the porous Teflon membrane. During the reaction, the gas components were pumped through the membrane and collected by DEMS for the fast detection of gas products. Before the DAT-OCD tests, a control experiment of the OER test in 1.0 M KOH without the addition of DAT was carried out using LSV over the potential range of 0.7−2.2 V vs RHE for three cycles (Figure S19a). As expected, the mass signal for m/z = 32 (O_2) was detected at 1.83 V, proving the poor OER activity of CuO@CF. In addition, the mass signal for m/z = 2 (H_2) was not detected, indicating that the hydrogen atoms in H_2O are not involved in the anodic H_2 evolution (Figure S19b). Then, the DEMS was performed in 1.0 M KOH + 0.2 M DAT over the potential range of 0.7−2.2 V vs RHE for the first two cycles (Figure 4e). Interestingly, the signal of m/z = 2 (H_2) shows an intense peak accompanied by strong fluctuation with numerous H_2 bubbles observed (Video S1), while the signal of m/z = 32 (O_2) was not detected even when the potential was shifted to the OER range (>1.83 V vs RHE). The cutoff potentials are then controlled to 1.4, 1.3, and 1.4 V for the third, fourth, and fifth to seventh cycles, respectively, to adjust the amount of H_2. This result indicates the high correlation between the applied potential and the amount of H_2: the higher the applied potential, the higher the amount of produced H_2. Meanwhile, the competitive OER could be well inhibited to promote the Faradaic efficiency of DAT-OCD. The origin of H in H_2 was verified by an isotope labeling experiment.

The active hydrogen of amino in DAT was deuterated by immersing 0.2 M DAT in deuteroxide (Figure S20). The in situ DEMS spectra show that m/z = 4 (D_2) of gas products is detected, followed by a weak mass signal of m/z = 2 (H_2), which may be due to the incomplete deuteration of amino in DAT. When the concentration of DAT was reduced to 0.1 M, the complete deuteration is supported by ^1H nuclear magnetic resonance (NMR) as evidenced by the disappearance of the H signal of DAT (Figure S21). As noted from Figure 4f, a strong signal for m/z = 4 (D_2) was detected, whereas there were no signals of m/z = 2 (H_2), m/z = 3 (HD), and m/z = 32 (O_2), suggesting that all of the D atoms in D_2 originated from the deuterated amino group in the DAT substrate, with no O_2 formation in the process. In other words, the competitive OER and Heyrovsky pathway are not involved in the DAT-OCD. Note that the detection of a negative signal of m/z = 32 is due to the H_2 fluctuation in the sampled gaseous mixture for the DEMS analysis. Based on the above discussion and in situ ATR-FTIR (Figure S18), it can be demonstrated that the H_2 production mechanism at the anode is the dehydrogenation of the amino group triggered by OH*, and the produced H* from two DAT molecules recombine to form H_2 via the Tafel pathway, rather than the Heyrovsky or Volmer step (produce nonvalued H_2O), leading to satisfactory atom efficiency of the bipolar hydrogen production by anodic N−N oxidatively coupled dehydrogenation and HER.

In situ ATR-FTIR spectroscopy was performed to further verify the dehydrogenation and H_2 production mechanism of DAT-OCD. The spectra were collected by applying various potentials via chronoamperometry between 0.7 and 1.45 V vs RHE without the competitive OER process (Figure 4g). The large vibration bands at ~1593 cm^{-1} are attributed to the $-NH_2$ groups of the DAT substrate.[75] It can be seen that the peak of $-NH_2$ appears at a potential of 0.85 V vs RHE in accord with the onset potential of DAT-OCD in the LSV test (Figure 4a), indicating that the oxidation of DAT begins at an ultralow potential input than that of OER. The pronounced growth of the $-NH_2$ peak with an increase in the applied potential suggests that more DAT substrate was adsorbed on the surface of CuO and promotes the kinetics of DAT-OCD. The vibration bands at ~1284 cm^{-1} originated from the N−NH/C−N vibration within the triazole rings in DAT.[84] Meanwhile, we observed weak growth of the peaks at 1435 and 1485 cm^{-1}, respectively, assigned to −C═N− and −N═N− vibrations.[75] The similar peak intensity variation trends of −C═N− and those of −N═N− and −NH−NH− with the increase of potential is attributed to the fast kinetics of DAT-OCD. At a relatively low applied potential, the DAT-OCD reaction did not occur due to kinetic limitations, presenting no apparent signal of the vibration bands. When the applied potential was increased, the DAT-OCD reaction was triggered, and the adsorption signals of $-NH_2$ and −C═N− bonds over the DAT substrate were detected. Meanwhile, the formation of −N═N− bonds was also detected due to the fast kinetics of the DAT-OCD reaction. On the other hand, the adsorption of the DAT substrate on the CuO surface was also enhanced with the increasing potential, leading to a similar trend of −C═N− bonding to those of −N═N− and −NH−NH− bonding. In contrast, ATR-FTIR of the OER without the addition of DAT (Figure S22a) shows no apparent peak intensity variations with

https://doi.org/10.1021/jacs.4c17225
J. Am. Chem. Soc. 2025, 147, 9505−9518

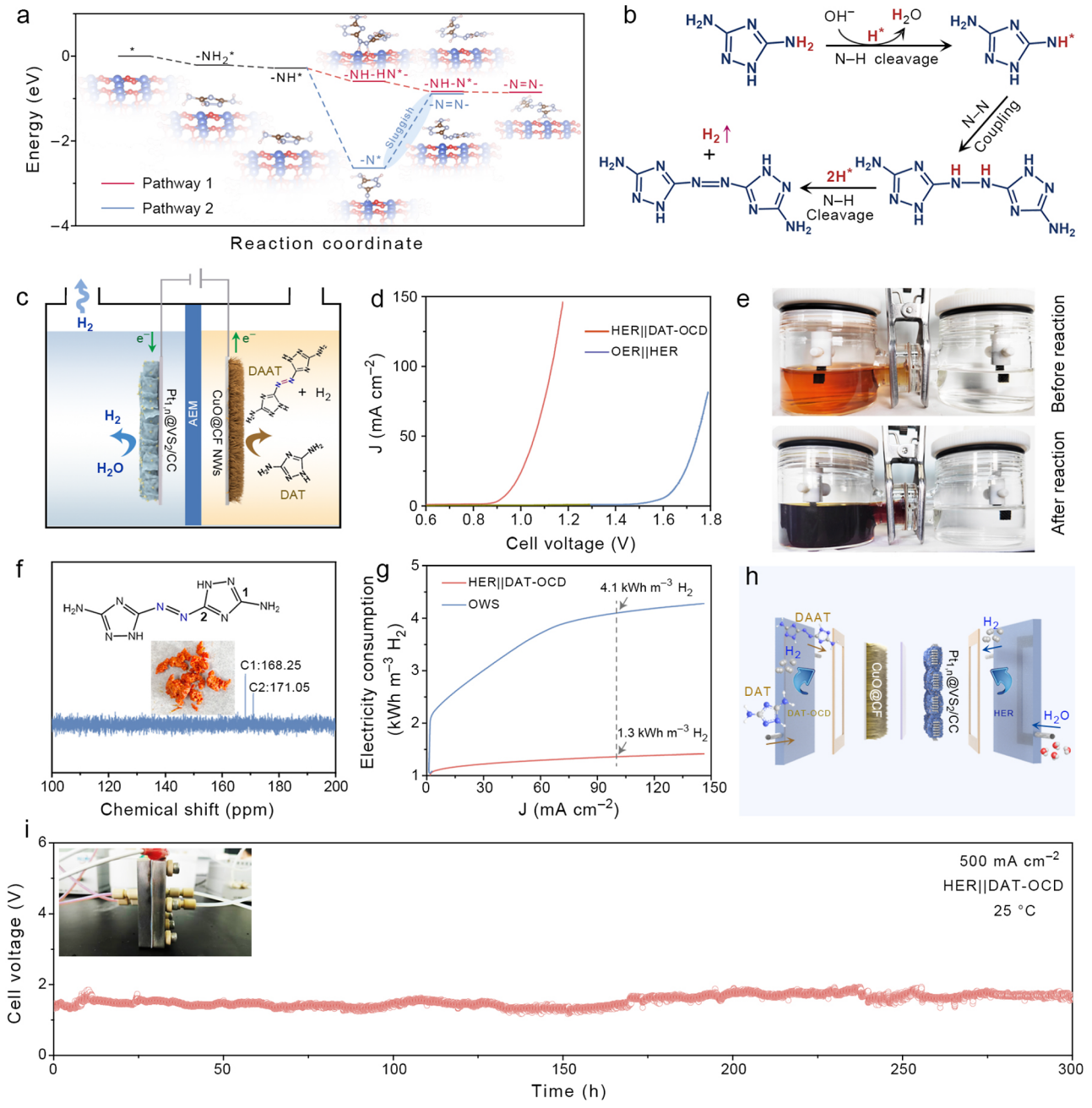

Figure 5. (a) Relative energy of a possible DAT-OCD pathway. (b) Proposed DAT-OCD mechanism on CuO@CF NWs. (c) Schematic illustration of the H-type cell for HER||DAT-OCD. (d) LSV curves of the traditional OWS and coupling system of HER||DAT-OCD. (e) Optical image of the coupling system before and after the long-term stability test. (f) ^{13}C NMR spectrum of DAAT products. (g) Consumed electricity analysis of the OWS and HER||DAT-OCD. (h) Schematic illustration of an AEM electrolyzer. (i) Long-term stability test of the HER||DAT-OCD AEM electrolyzer at 500 mA cm^{-2}.

the increase of the potential, indicating the successful synthesis of DAAT azo products.

Attention was then directed to the DAT-OCD mechanism. There are two main pathways in electrochemical organic oxidation: electrochemical−chemical oxidation and OH* oxidation.[85] The former involves the reaction of OH^- with the catalyst surface to form high-valence derivatives as the active sites, which activate and oxidize the substrate molecules into target products, accompanied by the reduction of the catalyst to its initial state. The latter involves OH^- adsorption at a certain potential, forming OH* without the valence change of the catalyst. The OH* then activates nucleophilic groups (e.g., amino) to promote N−H cleavage and produce oxidation products and water molecules. Whether the OH^- participated in the DAT-OCD was verified by ATR-FTIR (Figures S18 and S22), where OH* was detected in both DAT-OCD and OER. This result suggests that OH* is involved in the DAT-OCD reaction. Hence, the OH* oxidation mechanism dominates the DAT-OCD reaction. Besides, the upward peaks at 1720 and 1665 cm^{-1} correspond to −NH−NH− coupling bonds.[86]

DFT calculations were implemented to further verify the possible direct electrooxidation pathway for DAT-OCD (Figure 5a). Compared with the adsorption energy (E_{ads}) of the vertically aligned DAT molecule on CuO (E_{ads} = 0.3 eV)

https://doi.org/10.1021/jacs.4c17225
J. Am. Chem. Soc. 2025, 147, 9505−9518

(Figure S23), the horizontally aligned DAT molecule exhibits a lower E_{ads} (−0.21 eV), which is used as a model structure for the following calculations. All of the dehydrogenation and −NH−NH− coupling steps are exothermic processes in pathway 1, while the sluggish step is observed on −N* and −N* coupling to form −N═N− final products in pathway 2, indicating that pathway 1 dominates the DAT-OCD process. In addition, the free energies of amino dehydrogenation of DAT molecules on Cu and $Cu(OH)_2$ were assessed by DFT calculations. As shown in Figure S24, the free energies of amino dehydrogenation on Cu and $Cu(OH)_2$ were 2.03 and 2.25 eV, respectively, while the amino dehydrogenation was more favorable on CuO (−0.28 eV, Figure 5a), suggesting a weak amino dehydrogenation capacity on Cu and $Cu(OH)_2$ catalysts. It is noted that the O−H in $Cu(OH)_2$ tends to dissociate and the produced H* bonds with dehydrogenated animo to form a DAT molecule, indicating that the dehydrogenation of DAT was thermodynamically unfavorable on these catalysts. This may be the reason for the enhanced DAT-OCD electrocatalytic activity on CuO@CF, which is consistent with the electrochemical results and the in situ ATR-FTIR analysis. Based on the above discussion, we propose that the main mechanistic pathway of dehydrogenation of the amino group driven by OH* in DAT yields −NH* intermediates and water molecules. Then, the −NH* reacts with another −NH* to achieve N−N oxidative coupling, leading to −NH−NH− intermediates. Finally, dehydrogenation proceeds further to yield the DAAT products, while the produced H* intermediates combine to form H_2 via the Tafel pathway (Figure 5b).

Water Electrolysis Device Performance. Encouraged by the superior electrocatalytic performance of HER and DAT-OCD, a two-electrode cell employing $Pt_{1,n}@VS_2$/CC and CuO@CF NWs as the cathode and anode electrodes was constructed, respectively (Figure 5c). The HER||DAT-OCD delivers ultralow cell voltages of 0.94 and 1.05 V to reach 10 and 50 mA cm^{-2}, respectively, remarkably lower than that of HER||OER (overall water splitting, OWS), where high cell voltages of 1.67 and 1.74 V are required at 10 and 50 mA cm^{-2}, respectively (Figure 5d). The excellent activity of HER||DAT-OCD is attributed to the low-potential N−N oxidative coupling reaction, which in turn increases the cathodic hydrogen production energy efficiency.

The stability after the third LSV test was determined, and the results are shown in Figure S25. CuO@CF exhibits no apparent morphology changes. The long-term stability of the H-type cell for HER||DAT-OCD is then determined at a current density of 10 mA cm^{-2} (Figure S26). The coupled system steadily operated for at least 300 h with negligible activity attenuation. The sudden voltage "drop" during the test is due to the supplementation of the DAT substrate, indicating the DAT-OCD is crucial for low-energy H_2 production.

After the long-term stability reaction, the color of the anodic electrolyte changes from orange red to crimson (Figure 5e). The obtained anodic electrolyte is then treated by acidification, hot filter, and vacuum drying (as detailed in the Experimental Section in the SI). The target orange-colored DAAT products were collected and characterized by NMR spectroscopy (Figure 5f). The two kinds of carbon environments located at the chemical shift of δ = 168.25 and 171.05 ppm are assigned to C−NH_2 and C−N═N species, respectively.[34] No other compounds, including dehydrogenation of the para position of amino to yield oligomers, are detected by ^{13}C NMR spectroscopy, indicating the successful synthesis of DAAT compounds (Figure S27). Benefiting from the bipolar hydrogen production on both anodic N−N oxidative dehydrogenation and cathodic hydrogen evolution, the electricity consumption of the coupling system only required 1.3 kWh m^{-3} H_2 at a current density of 100 mA cm^{-2}, which is one-third the electricity of conventional OWS (4.1 kWh m^{-3} H_2) to reach the same current density, saving ∼68% electricity input (Figure 5g).

Encouraged by the excellent performance of the bipolar hydrogen production system, we further assembled an anion-exchange membrane (AEM) electrolyzer to evaluate the industrial potential of our bipolar hydrogen production DAT-OCD||HER system using CuO@CF NWs and $Pt_{1,n}@VS_2$/CC as the anode and cathode, respectively (Figure 5h). The long-term stability of the AEM electrolyzer is tested at a current density of 500 mA cm^{-2}, demonstrating the excellent durability over 300 h with negligible activity decay (Figure 5i). The Faradaic efficiency (FE) of anodic DAT-OCD was calculated at various current densities (Figure S28). The FE was maintained at a high level of >90% over a wide current density range. The DAT-OCD can also deliver a high FE of 90.8% at a large current density of 500 mA cm^{-2}. The commendable performance of the DAT-OCD||HER system suggests the potential of the industrialized alkaline water electrolyzer.

CONCLUSIONS

A hybrid low-potential electrolyzer system was successfully developed, combining an N−N oxidatively coupled dehydrogenation reaction of the amino group in aminoazole substrates and the usual HER for anodic and cathodic hydrogen productions, respectively. An ultralow potential of 0.87 V vs RHE is obtained for DAT-OCD at 10 mA cm^{-2}. In situ DEMS, isotope labeling tests, in situ ATR-FTIR spectroscopy, and DFT calculations confirm that hydrogen production during DAT-OCD and the H atoms in H_2 are all from the amino group in the DAT substrates. The N−H bond cleavage and −NH−NH− bridging followed by further dehydrogenation to form −N═N− dominate the reaction. Meanwhile, the H atoms from N−H bond cleavage are recombined through the Tafel pathway to form H_2. The cathodic alkaline HER is driven by highly efficient $Pt_{1,n}@VS_2$/CC electrocatalysts with a low η_{10} of 40.3 mV and a superior stability of 100 h. DFT calculations demonstrate the cascade catalysis of alkaline HER and that the Pt SAs sites of $Pt_{1,n}$ promote the Volmer step, which causes H* to spill over to the S sites via the Heyrovsky pathway for fast hydrogen production.

A coupled H-type electrolysis system was assembled, and ultralow cell voltages of 0.94 and 1.05 V were required to reach 10 and 50 mA cm^{-2}, respectively. Consequently, this coupled system only requires one-third of the electricity of the conventional OWS. Remarkably, a hybrid flow cell of the AEM device with DAT-OCD||HER shows robust stability at 500 mA cm^{-2} for 300 h, revealing great promise of the hybrid system for large-scale applications. Given the low-potential N−N oxidative dehydrogenation for hydrogen production at the anode, we anticipate that this bipolar hydrogen production system will be applicable to many amino group-based dehydrogenation processes for low-energy hydrogen production, as well as value-added azo chemicals from the anode.

https://doi.org/10.1021/jacs.4c17225
J. Am. Chem. Soc. 2025, 147, 9505−9518

■ ASSOCIATED CONTENT

Supporting Information

The Supporting Information is available free of charge at https://pubs.acs.org/doi/10.1021/jacs.4c17225.

Additional experimental details, materials, and methods; SEM and TEM images of VS_2@CC; EPR, contact angle tests, XPS of $Pt_{1,n}$@VS_2/CC and VS_2/CC; EDTA and KSCN poison test of HER; structural models of VS_2-supported Pt_1, Pt_n, and $Pt_{1,n}$; structural models of H* adsorption and water dissociation sites on Pt_1@VS_2, Pt_n@VS_2, and $Pt_{1,n}$@VS_2; in situ SERS of HER at various potentials; in situ ATR-FTIR spectra of DAT-OCD and OER; SEM image of $Cu(OH)_2$@CF; XRD pattern of CuO@CF; in situ DEMS of OER and DAT-OCD; ^1H and ^{13}C NMR spectra of DAT and DAAT; CP test of the H-type coupled system; FE of DAT-OCD; table of Pt L_3-edge EXAFS fitting parameters for all samples; table of comparison of applied potential for DAT-OCD with references (PDF)

Anodic H_2 production from DAT-OCD (MP4)

■ AUTHOR INFORMATION

Corresponding Authors

Ming Xu − *College of Chemistry, Chemical Engineering and Resource Utilization, Center for Innovative Research in Synthetic Chemistry and Resource Utilization, Northeast Forestry University, Harbin 150040, China*; Email: mingxu@nefu.edu.cn

Haixia Ma − *Xi'an Key Laboratory of Special Energy Materials, School of Chemical Engineering, Northwest University, Xi'an 710127, China; Zhijian Laboratory, Xi'an 710025, China*; orcid.org/0000-0001-9080-2004; Email: mahx@nwu.edu.cn

Jieshan Qiu − *State Key Laboratory of Chemical Resource Engineering, College of Chemical Engineering, Beijing University of Chemical Technology, Beijing 100029, China*; orcid.org/0000-0002-6892-6665; Email: qiujs@mail.buct.edu.cn

Zhengxiao Guo − *Department of Chemistry, The University of Hong Kong, Hong Kong 999077 SAR, China*; orcid.org/0000-0001-5404-3215; Email: zxguo@hku.hk

Authors

Jiachen Li − *Xi'an Key Laboratory of Special Energy Materials, School of Chemical Engineering, Northwest University, Xi'an 710127, China; Department of Chemistry, The University of Hong Kong, Hong Kong 999077 SAR, China*

Yang Li − *Shaanxi Key Laboratory of Degradable Biomedical Materials, School of Chemical Engineering, Northwest University, Xi'an 710127, China*

Yuqiang Ma − *Xi'an Key Laboratory of Special Energy Materials, School of Chemical Engineering, Northwest University, Xi'an 710127, China*

Zihang Zhao − *Xi'an Key Laboratory of Special Energy Materials, School of Chemical Engineering, Northwest University, Xi'an 710127, China*

Huarong Peng − *Department of Chemistry, The University of Hong Kong, Hong Kong 999077 SAR, China*

Tao Zhou − *Department of Chemistry, The University of Hong Kong, Hong Kong 999077 SAR, China*

Daidi Fan − *Shaanxi Key Laboratory of Degradable Biomedical Materials, School of Chemical Engineering, Northwest University, Xi'an 710127, China*; orcid.org/0000-0001-9798-1674

Complete contact information is available at: https://pubs.acs.org/10.1021/jacs.4c17225

Author Contributions

[▽]J.L. and Y.L. contributed equally to this work.

Notes

The authors declare no competing financial interest.

■ ACKNOWLEDGMENTS

The authors acknowledge support from the Hong Kong Scholar Program (XJ2023009), the HK RGC-GRF Grant (17300424), UGC-TRS (T23-713/22-R) award, the HK Environment and Conservation Fund (ECF 2021-152; ECF2021-141), the European Union-Hong Kong Research Cooperation Co-funding Mechanism by the Research Grants Council sponsored by the Research Grants Council (E-HKU701/23 and GH2-101070721), the Shaanxi Key Science and Technology Innovation Team Project (2022TD-33), the Shaanxi Key Research and Development Project (2024GX-YBXM-452), the Postdoctoral Research Project of Shaanxi (2023BSHYDZZ137), the Young Elite Scientists Sponsorship Program by Xi'an Association for Science and Technology (959202313084), and the Zhijian Laboratory Program (2024-ZJSYS-KF02-03). The authors thank Dr. Zihan Shen for the support of VASP calculations and data analysis. The authors are thankful for the support of the Beijing Synchrotron Radiation Facility (BSRF) during the XAFS measurements at the beamline 1W1B, 4B7A, 4B7B, 4B9A, and 4B9B.

■ REFERENCES

(1) Cheng, G.; Yang, Y.; Xiu, T.; Chen, B.; Zhao, T.; Wang, X.; Dong, C.; Zhao, Y. Analysis of Hydrogen Production Potential from Water Electrolysis in China. *Energy Fuels* **2023**, *37* (13), 9220−9232.

(2) Quan, L.; Jiang, H.; Mei, G.; Sun, Y.; You, B. Bifunctional Electrocatalysts for Overall and Hybrid Water Splitting. *Chem. Rev.* **2024**, *124* (7), 3694−3812.

(3) Badreldin, A.; Youssef, E.; Djire, A.; Abdala, A.; Abdel-Wahab, A. A Critical Look at Alternative Oxidation Reactions for Hydrogen Production from Water Electrolysis. *Cell Reports Phys. Sci.* **2023**, *4* (6), No. 101427.

(4) Wang, T.; Tao, L.; Zhu, X.; Chen, C.; Chen, W.; Du, S.; Zhou, Y.; Zhou, B.; Wang, D.; Xie, C.; Long, P.; Li, W.; Wang, Y.; Chen, R.; Zou, Y.; Fu, X. Z.; Li, Y.; Duan, X.; Wang, S. Combined Anodic and Cathodic Hydrogen Production from Aldehyde Oxidation and Hydrogen Evolution Reaction. *Nat. Catal.* **2022**, *5* (1), 66−73.

(5) Sun, H.; Xu, X.; Fei, L.; Zhou, W.; Shao, Z. Electrochemical Oxidation of Small Molecules for Energy-Saving Hydrogen Production. *Adv. Energy Mater.* **2024**, *14*, No. 2401242.

(6) Qian, Q.; Zhu, Y.; Ahmad, N.; Feng, Y.; Zhang, H.; Cheng, M.; Liu, H.; Xiao, C.; Zhang, G.; Xie, Y. Recent Advancements in Electrochemical Hydrogen Production via Hybrid Water Splitting. *Adv. Mater.* **2024**, *36*, No. 2306108.

(7) Ren, J. T.; Chen, L.; Wang, H. Y.; Tian, W. W.; Yuan, Z. Y. Water Electrolysis for Hydrogen Production: From Hybrid Systems to Self-Powered/Catalyzed Devices. *Energy Environ. Sci.* **2024**, *17*, 49−113.

(8) Xu, K.; Liang, L.; Li, T.; Bao, M.; Yu, Z.; Wang, J.; Thalluri, S. M.; Lin, F.; Liu, Q.; Cui, Z.; Song, S.; Liu, L. $Pt_{1.8}Pd_{0.2}$CuGa Intermetallic Nanocatalysts with Enhanced Methanol Oxidation Performance for Efficient Hybrid Seawater Electrolysis. *Adv. Mater.* **2024**, *36*, No. 2403792.

(9) Li, Z.; Yan, Y.; Xu, S.-M.; Zhou, H.; Xu, M.; Ma, L.; Shao, M.; Kong, X.; Wang, B.; Zheng, L.; Duan, H. Alcohols Electrooxidation Coupled with H_2 Production at High Current Densities Promoted by a Cooperative Catalyst. *Nat. Commun.* **2022**, *13* (1), 147.
(10) Yu, H.; Hu, M.; Chen, C.; Hu, C.; Li, Q.; Hu, F.; Peng, S.; Ma, J. Ambient γ-Rays-Mediated Noble-Metal Deposition on Defect-Rich Manganese Oxide for Glycerol-Assisted H_2 Evolution at Industrial-Level Current Density. *Angew. Chem., Int. Ed.* **2023**, *62* (52), No. e202314569.
(11) Han, G.; Li, G.; Sun, Y. Electrocatalytic Dual Hydrogenation of Organic Substrates with a Faradaic Efficiency Approaching 200%. *Nat. Catal.* **2023**, *6*, 224−233.
(12) Li, G.; Han, G.; Wang, L.; Cui, X.; Moehring, N. K.; Kidambi, P. R.; Jiang, D. en; Sun, Y. Dual Hydrogen Production from Electrocatalytic Water Reduction Coupled with Formaldehyde Oxidation via a Copper-Silver Electrocatalyst. *Nat. Commun.* **2023**, *14* (1), 525.
(13) Pan, X.; Sun, L.; Zhou, Z.; Xie, Y.; Zheng, J.; Xu, S.; Sun, J.; Zeng, J.; Zhao, G. Positive Electronic Nickel Active Site Enhances N−H/C−H Bonds Breaking for Electrooxidation of Amines to Nitriles Coupling with Hydrogen Production. *Adv. Energy Mater.* **2024**, *14*, No. 2400374.
(14) Sun, L.; Zhou, Z.; Xie, Y.; Zheng, J.; Pan, X.; Li, L.; Zhao, G. Surface Self-Reconstruction of Fe-Ni_3S_2 Electrocatalyst for Value-Generating Nitrile Evolution Reaction to Drive Efficient Hydrogen Production. *Adv. Funct. Mater.* **2023**, *33*, No. 2301884.
(15) Zhang, C.; Ma, Y.; Zhang, C.; Guo, Z.; Mu, X.; Liu, N.; Wang, X.; Li, J.; Xu, M.; Ma, H. Electrochemical Oxidation Synthesis of Energetic Compound Coupled with Energy-Efficient Hydrogen Evolution. *Electrochim. Acta* **2024**, *507*, No. 145164.
(16) Du, M.; Ji, Y.; Li, Y.; Liu, S.; Yan, J. Construction of an Internal Charge Field: $CoS_{1.097}/Ni_3S_2$ Heterojunction Promotes Efficient Urea Oxidation Reaction. *Adv. Funct. Mater.* **2024**, *34*, No. 2402776.
(17) Xu, S.; Jiao, D.; Ruan, X.; Jin, Z.; Qiu, Y.; Feng, Z.; Zheng, L.; Fan, J.; Zheng, W.; Cui, X. O-2p Hybridization Enhanced Transformation of Active γ-NiOOH by Chromium Doping for Efficient Urea Oxidation Reaction. *Adv. Funct. Mater.* **2024**, *34*, No. 2401265.
(18) Geng, S. K.; Zheng, Y.; Li, S. Q.; Su, H.; Zhao, X.; Hu, J.; Shu, H. B.; Jaroniec, M.; Chen, P.; Liu, Q. H.; Qiao, S. Z. Nickel Ferrocyanide as a High-Performance Urea Oxidation Electrocatalyst. *Nat. Energy* **2021**, *6* (9), 904−912.
(19) Li, J.; Li, Y.; Wang, J.; Zhang, C.; Ma, H.; Zhu, C.; Fan, D.; Guo, Z.; Xu, M.; Wang, Y.; Ma, H. Elucidating the Critical Role of Ruthenium Single Atom Sites in Water Dissociation and Dehydrogenation Behaviors for Robust Hydrazine Oxidation-Boosted Alkaline Hydrogen Evolution. *Adv. Funct. Mater.* **2022**, *32* (16), No. 2109439.
(20) Li, Y.; Niu, S.; Liu, P.; Pan, R.; Zhang, H.; Ahmad, N.; Shi, Y.; Liang, X.; Cheng, M.; Chen, S.; Du, J.; Hu, M.; Wang, D.; Chen, W.; Li, Y. Ruthenium Nanoclusters and Single Atoms on A-MoC/N-Doped Carbon Achieves Low-input/Input-free Hydrogen Evolution via Decoupled/Coupled Hydrazine Oxidation. *Angew. Chem., Int. Ed.* **2024**, *63*, No. e202316755.
(21) Zhu, Y.; Chen, Y.; Feng, Y.; Meng, X.; Xia, J.; Zhang, G. Constructing Ru-O-TM Bridge in NiFe-LDH Enables High Current Hydrazine-Assisted H2 Production. *Adv. Mater.* **2024**, *36*, No. 2401694.
(22) Lv, F.; Wu, J.; Liu, X.; Zheng, Z.; Pan, L.; Zheng, X.; Guo, L.; Chen, Y. Decoupled Electrolysis for Hydrogen Production and Hydrazine Oxidation via High-Capacity and Stable Pre-Protonated Vanadium Hexacyanoferrate. *Nat. Commun.* **2024**, *15* (1), 1339.
(23) Wang, J.; Zhou, M.; Fu, R.; Ge, J.; Yang, W.; Hong, X.; Sun, C.; Liao, X.; Zhao, Y.; Wang, Z. Iron Molybdenum Sulfide-Supported Ultrafine Ru Nanoclusters for Robust Sulfion Degradation-Assisted Hydrogen Production. *Adv. Funct. Mater.* **2024**, *34*, No. 2315326.
(24) Ren, J. T.; Chen, L.; Wang, H. Y.; Tian, W.; Wang, L.; Sun, M.; Feng, Y.; Zhai, S. X.; Yuan, Z. Y. Self-Powered Hydrogen Production with Improved Energy Efficiency via Polysulfides Redox. *ACS Nano* **2023**, *17* (24), 25707−25720.
(25) Chen, G.; Li, X.; Feng, X. Upgrading Organic Compounds through the Coupling of Electrooxidation with Hydrogen Evolution. *Angew. Chem., Int. Ed.* **2022**, *61* (42), No. e202209014.
(26) Yang, M.; Jiang, Y.; Dong, C.; Xu, L.; Huang, Y.; Leng, S.; Wu, Y.; Luo, Y.; Chen, W.; Thi, T.; Nga, T.; Wang, S.; Zou, Y. A Self-Reactivated PdCu Catalyst for Aldehyde Electro-Oxidation with Anodic Hydrogen Production. *Nat. Commun.* **2024**, *15*, 9852.
(27) Zhang, C.; Jiao, N. Copper-Catalyzed Aerobic Oxidative Dehydrogenative Coupling of Anilines Leading to Aromatic Azo Compounds Using Dioxygen as an Oxidant. *Angew. Chem.* **2010**, *122* (35), 6310−6313.
(28) Gao, H.; Shreeve, J. M. Azole-Based Energetic Salts. *Chem. Rev.* **2011**, *111* (11), 7377−7436.
(29) Yu, Q.; Staples, R. J.; Shreeve, J. M. An Azo-Bridged Triazole Derived from Tetrazine. *Zeitschrift fur Anorg. und Allg. Chem.* **2020**, *646* (22), 1799−1804.
(30) Xie, M.; Gong, J.; Zhou, J.; Wang, J.; Cao, Y.; Zhou, T.; Dai, Y. Green Coupling of 3,5-Diamino-1H-1,2,4-Triazole into the Azo Compound. *Mendeleev Commun.* **2023**, *33* (5), 717−720.
(31) Yount, J. R.; Zeller, M.; Byrd, E. F. C.; Piercey, D. G. 4,4′,5,5′-Tetraamino-3,3′-Azo-Bis-1,2,4-Triazole and the Electrosynthesis of High-Performing Insensitive Energetic Materials. *J. Mater. Chem. A* **2020**, *8* (37), 19337−19347.
(32) Yount, J.; Piercey, D. G. Electrochemical Synthesis of High-Nitrogen Materials and Energetic Materials. *Chem. Rev.* **2022**, *122* (9), 8809−8840.
(33) Yuan, Y.; Lei, A. Electrochemical Oxidative Cross-Coupling with Hydrogen Evolution Reactions. *Acc. Chem. Res.* **2019**, *52* (12), 3309−3324.
(34) Dippold, A.; Klapötke, T. M.; Martin, F. A. Synthesis and Characterization of Bis(Triaminoguanidinium) 5,5′-Dinitrimino-3,3′-Azo-1H-1,2,4-Triazolate-A Novel Insensitive Energetic Material. *Zeitschrift fur Anorg. und Allg. Chem.* **2011**, *637* (9), 1181−1193.
(35) Sun, L.; Pan, X.; Xie, Y. N.; Zheng, J.; Xu, S.; Li, L.; Zhao, G. Accelerated Dynamic Reconstruction in Metal−Organic Frameworks with Ligand Defects for Selective Electrooxidation of Amines to Azos Coupling with Hydrogen Production. *Angew. Chem., Int. Ed.* **2024**, *63* (2), No. 202402176.
(36) He, H.; Du, J.; Wu, B.; Duan, X.; Zhou, Y.; Ke, G.; Huo, T.; Ren, Q.; Bian, L.; Dong, F. Photoelectrochemical Driving and Clean Synthesis of Energetic Salts of 5,5′-Azotetrazolate at Room Temperature. *Green Chem.* **2018**, *20* (16), 3722−3726.
(37) Wang, F.; Yang, J.; Li, J.; Han, Y.; Li, A.; Xu, R.; Feng, X.; Wang, T.; Tong, C.; Li, J.; Wei, Z. Which Is Best for ORR: Single Atoms, Nanoclusters, or Coexistence? *ACS Energy Lett.* **2024**, *9*, 93−101.
(38) Mo, F.; Zhou, Q.; Xue, W.; Liu, W.; Xu, S.; Hou, Z.; Wang, J.; Wang, Q. The Optimized Catalytic Performance of Single-Atom Catalysts by Incorporating Atomic Clusters or Nanoparticles: In-Depth Understanding on Their Synergisms. *Adv. Energy Mater.* **2023**, *13* (38), No. 2301711.
(39) Chen, R.; Chen, S.; Wang, L.; Wang, D. Nanoscale Metal Particle Modified Single-Atom Catalyst: Synthesis, Characterization, and Application. *Adv. Mater.* **2023**, *36*, No. 2304713.
(40) Tian, Y.; Luo, Y.; Wu, T.; Quan, X.; Li, W.; Wei, G.; Bayati, M.; Wu, Q.; Fu, Y.; Wen, M. Coupling Interaction between Precisely Located Pt Single-Atoms/Clusters and NiCo-Layered Double Oxide to Boost Hydrogen Evolution Reaction. *Adv. Funct. Mater.* **2024**, *34*, No. 2405919.
(41) Zhang, Y. C.; Zhao, M.; Wu, J.; Wang, Y.; Zheng, L.; Gu, F.; Zou, J. J.; Gao, J.; Zhu, X. D. Construction of Pt Single-Atom and Cluster/FeOOH Synergistic Active Sites for Efficient Electrocatalytic Hydrogen Evolution Reaction. *ACS Catal.* **2024**, *14*, 7867−7876.
(42) Zhu, Y.; Fan, K.; Hsu, C. S.; Chen, G.; Chen, C.; Liu, T.; Lin, Z.; She, S.; Li, L.; Zhou, H.; Zhu, Y.; Chen, H. M.; Huang, H. Supported Ruthenium Single-Atom and Clustered Catalysts Outperform Benchmark Pt for Alkaline Hydrogen Evolution. *Adv. Mater.* **2023**, *35* (35), No. 2301133.

https://doi.org/10.1021/jacs.4c17225
J. Am. Chem. Soc. 2025, 147, 9505−9518

(43) Wang, K.; Cao, J.; Yang, X.; Sang, X.; Yao, S.; Xiang, R.; Yang, B.; Li, Z.; O'Carroll, T.; Zhang, Q.; Lei, L.; Wu, G.; Hou, Y. Kinetically Accelerating Elementary Steps via Bridged Ru-H State for the Hydrogen-Evolution in Anion-Exchange Membrane Electrolyzer. *Adv. Funct. Mater.* **2023**, *33* (16), No. 2212321.
(44) He, Q.; Zhou, Y.; Shou, H.; Wang, X.; Zhang, P.; Xu, W.; Qiao, S.; Wu, C.; Liu, H.; Liu, D.; Chen, S.; Long, R.; Qi, Z.; Wu, X.; Song, L. Synergic Reaction Kinetics over Adjacent Ruthenium Sites for Superb Hydrogen Generation in Alkaline Media. *Adv. Mater.* **2022**, *34* (20), No. 2110604.
(45) Su, P.; Pei, W.; Wang, X.; Ma, Y.; Jiang, Q.; Liang, J.; Zhou, S.; Zhao, J.; Liu, J.; Lu, G. Q. Max Exceptional Electrochemical HER Performance with Enhanced Electron Transfer between Ru Nanoparticles and Single Atoms Dispersed on a Carbon Substrate. *Angew. Chem., Int. Ed.* **2021**, *60*, 16044−16050.
(46) Yan, Q. Q.; Wu, D. X.; Chu, S. Q.; Chen, Z. Q.; Lin, Y.; Chen, M. X.; Zhang, J.; Wu, X. J.; Liang, H. W. Reversing the Charge Transfer between Platinum and Sulfur-Doped Carbon Support for Electrocatalytic Hydrogen Evolution. *Nat. Commun.* **2019**, *10* (1), 4977.
(47) Yang, W.; Li, M.; Zhang, B.; Liu, Y.; Zi, J.; Xiao, H.; Liu, X.; Lin, J.; Zhang, H.; Chen, J.; Wan, Z.; Li, Z.; Li, G.; Li, H.; Lian, Z. Interfacial Microenvironment Modulation Boosts Efficient Hydrogen Evolution Reaction in Neutral and Alkaline. *Adv. Funct. Mater.* **2023**, *33* (45), No. 2304852.
(48) Shi, Y.; Ma, Z. R.; Xiao, Y. Y.; Yin, Y. C.; Huang, W. M.; Huang, Z. C.; Zheng, Y. Z.; Mu, F. Y.; Huang, R.; Shi, G. Y.; Sun, Y. Y.; Xia, X. H.; Chen, W. Electronic Metal-Support Interaction Modulates Single-Atom Platinum Catalysis for Hydrogen Evolution Reaction. *Nat. Commun.* **2021**, *12* (1), 3021.
(49) Zhu, C.; Gao, D.; Ding, J.; Chao, D.; Wang, J. TMD-Based Highly Efficient Electrocatalysts Developed by Combined Computational and Experimental Approaches. *Chem. Soc. Rev.* **2018**, *47* (12), 4332−4356.
(50) Zhu, J.; Cai, L.; Yin, X.; Wang, Z.; Zhang, L.; Ma, H.; Ke, Y.; Du, Y.; Xi, S.; Wee, A. T. S.; Chai, Y.; Zhang, W. Enhanced Electrocatalytic Hydrogen Evolution Activity in Single-Atom Pt-Decorated VS_2 Nanosheets. *ACS Nano* **2020**, *14* (5), 5600−5608.
(51) Nam, G. H.; He, Q.; Wang, X.; Yu, Y.; Chen, J.; Zhang, K.; Yang, Z.; Hu, D.; Lai, Z.; Li, B.; Xiong, Q.; Zhang, Q.; Gu, L.; Zhang, H. In-Plane Anisotropic Properties of 1T′-MoS_2 Layers. *Adv. Mater.* **2019**, *31* (21), No. 1807764.
(52) Rhuy, D.; Lee, Y.; Kim, J. Y.; Kim, C.; Kwon, Y.; Preston, D. J.; Kim, I. S.; Odom, T. W.; Kang, K.; Lee, D.; Lee, W. K. Ultraefficient Electrocatalytic Hydrogen Evolution from Strain-Engineered, Multilayer MoS_2. *Nano Lett.* **2022**, *22* (14), 5742−5750.
(53) Tsai, C.; Li, H.; Park, S.; Park, J.; Han, H. S.; Nørskov, J. K.; Zheng, X.; Abild-Pedersen, F. Electrochemical Generation of Sulfur Vacancies in the Basal Plane of MoS_2 for Hydrogen Evolution. *Nat. Commun.* **2017**, *8*, No. 15113.
(54) Wu, F.; Yang, R.; Lu, S.; Du, W.; Zhang, B.; Shi, Y. Unveiling Partial Transformation and Activity Origin of Sulfur Vacancies for Hydrogen Evolution. *ACS Energy Lett.* **2022**, *7* (12), 4198−4203.
(55) Wang, M.; Feng, C.; Mi, W.; Guo, M.; Guan, Z.; Li, M.; Chen, H. C.; Liu, Y.; Pan, Y. Defect-Induced Electron Redistribution between Pt-N_3S_1 Single Atomic Sites and Pt Clusters for Synergistic Electrocatalytic Hydrogen Production with Ultra-High Mass Activity. *Adv. Funct. Mater.* **2024**, *34* (2), No. 2309474.
(56) Zhang, J.; Zhang, C.; Wang, Z.; Zhu, J.; Wen, Z.; Zhao, X.; Zhang, X.; Xu, J.; Lu, Z. Synergistic Interlayer and Defect Engineering in VS_2 Nanosheets toward Efficient Electrocatalytic Hydrogen Evolution Reaction. *Small* **2018**, *14* (9), No. 1703098.
(57) Zhou, Y.; Xu, Q.; Ge, T.; Zheng, X.; Zhang, L.; Yan, P. Accurate Control of VS_2 Nanosheets for Coexisting High Photoluminescence and Photothermal Conversion Efficiency. *Angew. Chem., Int. Ed.* **2020**, *59* (8), 3322−3328.
(58) Kwon, I. S.; Kwak, I. H.; Debela, T. T.; Kim, J. Y.; Yoo, S. J.; Kim, J. G.; Park, J.; Kang, H. S. Phase-Transition $Mo_{1-X}V_xSe_2$ Alloy Nanosheets with Rich V-Se Vacancies and Their Enhanced Catalytic Performance of Hydrogen Evolution Reaction. *ACS Nano* **2021**, *15* (9), 14672−14682.
(59) Ihsan, J.; Kwak, I. H.; Kim, J. Y.; Zewdie, G. M.; Choi, J. H.; Lee, S. G.; Lee, K. S.; Kwon, I. S.; Park, J.; Kang, H. S. Alloying of ReS_2 and VS_2 Nanosheets Enhances Electrocatalytic Hydrogen Evolution Reaction. *Adv. Funct. Mater.* **2024**, *34*, No. 2406755.
(60) Qi, K.; Cui, X.; Gu, L.; Yu, S.; Fan, X.; Luo, M.; Xu, S.; Li, N.; Zheng, L.; Zhang, Q.; Ma, J.; Gong, Y.; Lv, F.; Wang, K.; Huang, H.; Zhang, W.; Guo, S.; Zheng, W.; Liu, P. Single-Atom Cobalt Array Bound to Distorted 1T Evolution Catalysis MoS_2 with Ensemble Effect for Hydrogen. *Nat. Commun.* **2019**, *10*, 5231.
(61) Jiang, K.; Luo, M.; Liu, Z.; Peng, M.; Chen, D.; Lu, Y. R.; Chan, T. S.; de Groot, F. M. F.; Tan, Y. Rational Strain Engineering of Single-Atom Ruthenium on Nanoporous MoS_2 for Highly Efficient Hydrogen Evolution. *Nat. Commun.* **2021**, *12* (1), 1687.
(62) Wei, S.; Cui, X.; Xu, Y.; Shang, B.; Zhang, Q.; Gu, L.; Fan, X.; Zheng, L.; Hou, C.; Huang, H.; Wen, S.; Zheng, W. Iridium-Triggered Phase Transition of MoS_2 Nanosheets Boosts Overall Water Splitting in Alkaline Media. *ACS Energy Lett.* **2019**, *4* (1), 368−374.
(63) Andaveh, R.; Darband, G. B.; Maleki, M.; Rouhaghdam, A. S. Superaerophobic/Superhydrophilic Surfaces as Advanced Electrocatalysts for the Hydrogen Evolution Reaction: A Comprehensive Review. *J. Mater. Chem. A* **2022**, *10* (10), 5147−5173.
(64) Shi, Y.; Zhang, B. Recent Advances in Transition Metal Phosphide Nanomaterials: Synthesis and Applications in Hydrogen Evolution Reaction. *Chem. Soc. Rev.* **2016**, *45* (6), 1529−1541.
(65) Zhang, R.; Li, Y.; Zhou, X.; Yu, A.; Huang, Q.; Xu, T.; Zhu, L.; Peng, P.; Song, S.; Echegoyen, L.; Li, F. F. Single-Atomic Platinum on Fullerene C_{60} Surfaces for Accelerated Alkaline Hydrogen Evolution. *Nat. Commun.* **2023**, *14* (1), 2460.
(66) Greeley, J.; Jaramillo, T. F.; Bonde, J.; Chorkendorff, I.; Nørskov, J. K. Computational High-Throughput Screening of Electrocatalytic Materials for Hydrogen Evolution. *Nat. Mater.* **2006**, *5* (11), 909−913.
(67) Xie, L.; Wang, L.; Liu, X.; Chen, J.; Wen, X.; Zhao, W.; Liu, S.; Zhao, Q. Flexible Tungsten Disulfide Superstructure Engineering for Efficient Alkaline Hydrogen Evolution in Anion Exchange Membrane Water Electrolysers. *Nat. Commun.* **2024**, *15* (1), 5702.
(68) Chen, J.; Liu, G.; Zhu, Y. Z.; Su, M.; Yin, P.; Wu, X. J.; Lu, Q.; Tan, C.; Zhao, M.; Liu, Z.; Yang, W.; Li, H.; Nam, G. H.; Zhang, L.; Chen, Z.; Huang, X.; Radjenovic, P. M.; Huang, W.; Tian, Z. Q.; Li, J. F.; Zhang, H. Ag@MoS_2 Core-Shell Heterostructure as SERS Platform to Reveal the Hydrogen Evolution Active Sites of Single-Layer MoS_2. *J. Am. Chem. Soc.* **2020**, *142* (15), 7161−7167.
(69) Guo, S.; Li, Y.; Tang, S.; Zhang, Y.; Li, X.; Sobrido, A. J.; Titirici, M. M.; Wei, B. Monitoring Hydrogen Evolution Reaction Intermediates of Transition Metal Dichalcogenides via Operando Raman Spectroscopy. *Adv. Funct. Mater.* **2020**, *30* (35), No. 2003035.
(70) Shen, L.-F.; Lu, B.-A.; Li, Y.-Y.; Liu, J.; Huang-fu, Z.-C.; Peng, H.; Ye, J.-Y.; Qu, X.-M.; Zhang, J.-M.; Li, G.; Cai, W.-B.; Jiang, Y.-X.; Sun, S.-G. Interfacial Structure of Water as a New Descriptor of the Hydrogen Evolution Reaction. *Angew. Chem., Int. Ed.* **2020**, *59* (50), 22397−22402.
(71) Jeong, S.; Mai, H. D.; Nguyen, T. K.; Youn, J. S.; Nam, K. H.; Park, C. M.; Jeon, K. J. Atomic Interactions of Two-Dimensional PtS_2 Quantum Dots/TiC Heterostructures for Hydrogen Evolution Reaction. *Appl. Catal. B Environ.* **2021**, *293*, No. 120227.
(72) Meng, C.; Gao, Y.; Zhou, Y.; Sun, K.; Wang, Y.; Han, Y.; Zhao, Q.; Chen, X.; Hu, H.; Wu, M. P-Band Center Theory Guided Activation of MoS_2 Basal S Sites for pH Universal Hydrogen Evolution. *Nano Res.* **2023**, *16* (5), 6228−6236.
(73) Wang, L.; Gao, W.; Chen, X.; Liu, Y.; Qureshi, A. H.; Liu, Y.; Chen, M.; Zhang, X.; Guo, Y.; Wang, J. Charge-Modulated VS2Monolayer for Effective Hydrogen Evolution Reaction. *J. Phys. Chem. C* **2021**, *125* (22), 12004−12011.
(74) Zhou, P.; Lv, X.; Tao, S.; Wu, J.; Wang, H.; Wei, X.; Wang, T.; Zhou, B.; Lu, Y.; Frauenheim, T.; Fu, X.; Wang, S.; Zou, Y. Heterogeneous-Interface-Enhanced Adsorption of Organic and

https://doi.org/10.1021/jacs.4c17225
J. Am. Chem. Soc. 2025, 147, 9505−9518

Hydroxyl for Biomass Electrooxidation. *Adv. Mater.* **2022**, *34* (42), No. 2204089.
(75) Chellappa, R. S.; Dattelbaum, D. M.; Coe, J. D.; Velisavljevic, N.; Stevens, L. L.; Liu, Z. Intermolecular Stabilization of 3,3′-Diamino-4,4′-Azoxyfurazan (DAAF) Compressed to 20 GPa Raja. *J. Phys. Chem. A* **2014**, *118*, 5969−5982.
(76) Wang, T.; Zhang, Y.; Huang, B.; Cai, B.; Rao, R. R.; Giordano, L.; Sun, S. G.; Shao-Horn, Y. Enhancing Oxygen Reduction Electrocatalysis by Tuning Interfacial Hydrogen Bonds. *Nat. Catal.* **2021**, *4* (9), 753−762.
(77) Yang, M.; Li, Y.; Dong, C. L.; Li, S.; Xu, L.; Chen, W.; Wu, J.; Lu, Y.; Pan, Y.; Wu, Y.; Luo, Y.; Huang, Y. C.; Wang, S.; Zou, Y. Correlating the Valence State with the Adsorption Behavior of a Cu-Based Electrocatalyst for Furfural Oxidation with Anodic Hydrogen Production Reaction. *Adv. Mater.* **2023**, *35* (39), No. 2304203.
(78) Katayama, Y.; Okanishi, T.; Muroyama, H.; Matsui, T.; Eguchi, K. Enhanced Supply of Hydroxyl Species in CeO_2-Modified Platinum Catalyst Studied by in Situ ATR-FTIR Spectroscopy. *ACS Catal.* **2016**, *6* (3), 2026−2034.
(79) Zhou, Z.; Su, Y.; Tan, H.; Wang, Y.; Huang, Q.; Wang, H.; Wang, J.; Kubo, M.; Ni, Z.; Kong, Y.; Zhao, S. Atomically Dispersed Co-P Moieties via Direct Thermal Exfoliation for Alkaline Hydrogen Electrosynthesis. *J. Am. Chem. Soc.* **2025**, *147*, 3994.
(80) Zeng, L.; Chen, Y.; Sun, M.; Huang, Q.; Sun, K.; Ma, J.; Li, J.; Tan, H.; Li, M.; Pan, Y.; Liu, Y.; Luo, M.; Huang, B.; Guo, S. Cooperative Rh-O_5/Ni(Fe) Site for Efficient Biomass Upgrading Coupled with H_2 Production. *J. Am. Chem. Soc.* **2023**, *145* (32), 17577−17587.
(81) Fan, L.; Ji, Y.; Wang, G.; Chen, J.; Chen, K.; Liu, X.; Wen, Z. High Entropy Alloy Electrocatalytic Electrode toward Alkaline Glycerol Valorization Coupling with Acidic Hydrogen Production. *J. Am. Chem. Soc.* **2022**, *144* (16), 7224−7235.
(82) Zhu, B.; Dong, B.; Wang, F.; Yang, Q.; He, Y.; Zhang, C.; Jin, P.; Feng, L. Unraveling a Bifunctional Mechanism for Methanol-to-Formate Electro-Oxidation on Nickel-Based Hydroxides. *Nat. Commun.* **2023**, *14* (1), 1686.
(83) Ye, Y.; Xu, J.; Li, X.; Jian, Y.; Xie, F.; Chen, J.; Jin, Y.; Yu, X.; Lee, M. H.; Wang, N.; Sun, S.; Meng, H. Orbital Occupancy Modulation to Optimize Intermediate Absorption for Efficient Electrocatalysts in Water Electrolysis and Zinc−Ethanol−Air Battery. *Adv. Mater.* **2024**, *36*, No. 2312618.
(84) Franca, C. A.; Etcheverry, S. B.; Diez, R. P.; Williams, P. A. M. Irbesartan: FTIR and Raman Spectra. Density Functional Study on Vibrational and NMR Spectra. *J. Raman Spectrosc.* **2009**, *40* (9), 1296−1300.
(85) Wang, P.; Zheng, J.; Xu, X.; Zhang, Y. Q.; Shi, Q. F.; Wan, Y.; Ramakrishna, S.; Zhang, J.; Zhu, L.; Yokoshima, T.; Yamauchi, Y.; Long, Y. Z. Unlocking Efficient Hydrogen Production: Nucleophilic Oxidation Reactions Coupled with Water Splitting. *Adv. Mater.* **2024**, *36* (35), No. 2404806.
(86) Wang, H.; Jung, H.; Song, F.; Zhu, S.; Bai, Z.; Chen, D.; He, G.; Chang, S.; Chen, G. Nitrene-Mediated Intermolecular N−N Coupling for Efficient Synthesis of Hydrazides. *Nat. Chem.* **2021**, *13* (4), 378−385.

https://doi.org/10.1021/jacs.4c17225
J. Am. Chem. Soc. 2025, 147, 9505−9518